석사학위논문

Impacts of river-discharged freshwater on surface ocean environments revealed by multi-satellite measurements

강 소 영

제주대학교 대학원

지구해양융합학부 지구해양전공

2023년 8월

Impacts of river-discharged freshwater on surface ocean environments revealed by multi-satellite measurements

지도교수 문재홍

강 소 영

이 논문을 이학 석사학위 논문으로 신청함

2023년 8월

강소영의 이학 석사학위 논문을 인준함

심사위원장 송 상 근 印

위 원 김 정 현 印

위 원 문 재 홍 印

제주대학교 대학원

지구해양융합학부
지구해양전공

2023 년 8 월

Index

List of Figures

List of Tables

Abstract

River discharge forms a plume of low-salinity water that spreads offshore, delivering terrestrial substances into the ocean and thus plays a critical role in controlling marine environments as well as the carbon cycle. This study investigated how freshwater discharged from Changjiang impacts the physical and biological responses and oceanic uptake of carbon dioxide (CO_2) in the northern East China Sea (ECS) by combining the recently available sea surface salinity (SSS) product from the Soil Moisture Active Passive (SMAP) mission with other satellite measurements of sea surface temperature (SST) and chlorophyll-a (*chl-a*) concentration. The partial pressure of CO_2 (pCO_2) and its interannual variability were estimated using empirical regression with satellite-derived environmental variables. The bias-corrected SMAP SSS revealed that river discharge largely contributed to the distinct interannual SSS variations, with a seasonal cycle reaching a maximum in winter and a minimum in summer. Compared to the SST and *chl-a* anomalies, we observed an increase in SST and primary production in the region where sea surface freshening was robust. Freshwater from rivers contributes to sea surface warming by trapping heat from the atmosphere at the surface layer. Nutrient-enriched freshwater within the buoyant plume enhances phytoplankton production, which in turn enriches the ocean surface with *chl-a*. Simultaneously, the pCO_2 was relatively low in the region where the SST and primary production were high, highlighting that the heat and riverine nutrients trapped within the buoyant plume contributed to the reduction in pCO_2 by promoting the biological uptake of CO_2. The estimates conducted here illustrate the synergistic utility of multiple satellite measurements for the evaluation of CO_2 uptake capacity, complemented by in situ measurements of river-dominated marginal seas.

1. Introduction

River discharge forms buoyant freshwater plumes that spread offshore and supply large amounts of nutrients and organic matter to the open ocean. The spread of freshwater dominates the spatial and temporal structure of sea-surface salinity (SSS) by mixing with ambient saline water, which is an important factor in the hydrological cycle and physical oceanic processes (Yu, 2011; Moon and Song, 2014). From a physical perspective, low-salinity water discharged from rivers often drives significant coastal current systems owing to buoyancy in the plume, which alters the wind-driven circulation (Whitney and Garvine, 2005; Wu et al., 2013). Salinity-induced stratification greatly influences heat exchange between the surface and subsurface layers, frequently resulting in a significant increase in the sea surface temperature (SST) over the freshening area (Foltz and McPhaden, 2009; Kako et al., 2016; Fournier et al., 2017; Moon et al., 2019). In addition, enhanced SST warming often contributes to the intensification of tropical cyclones that pass over freshening regions by exchanging heat and moisture at the air-sea interface (Balaguru et al., 2012; Hong et al., 2022). Regarding the biological aspects, discharged riverine materials, including terrestrial organic carbon, can significantly affect marine environments in response to interactions between physical, biological, and chemical processes, thereby playing an important role in both the ecosystem and the carbon cycle (Cai and Dai, 2004; Borges et al., 2015; Bai et al., 2015; Dai et al., 2022; Liu et al; 2022). Therefore, river-driven SSS can be an important variable in tracing the transport of riverine materials into the ocean and diagnosing ocean mixing and stratification.

The East China Sea (ECS) is a river-dominated marginal sea located in the northwestern Pacific Ocean (Fig. 1). As a major source of freshwater, the Changjiang (also known as the Yangtze River), which is the world's fifth largest river, contributes to ~ 90% of the entire

river discharge into the ECS (Beardsley et al., 1985), delivering large amounts of terrestrial substances (e.g., nutrients, organic, and inorganic carbon) into the ocean. In summer, the outflow of buoyant freshwater remains on top of the shelf water and spreads several hundreds of kilometers offshore toward the central ECS shelf, diluting the ambient shelf water (Beardsley et al., 1985; Lie et al., 2003), which is called the Changjiang Diluted Water (CDW). The offshore spreading of the CDW has been simulated in numerous ocean modeling studies (e.g., Chang and Isobe, 2003; Moon et al., 2009a, 2010, 2012; Hong et al., 2016). Recently, Moon et al. (2019) detected strong SST warming over the northern ECS in the summer of 2016, corresponding to a significant freshening area. Based on the results of numerical experiments, they showed that the CDW-induced barrier layer formation could be attributed to enhanced sea-surface warming over areas where surface freshening was significant. A close relationship between river-driven freshening and the partial pressure of carbon dioxide (pCO_2) was recently reported by Choi et al. (2021), who showed that biological processes promoted by nutrient-rich freshwater can contribute to a reduction in surface pCO_2 uptake based on a shipboard survey in August 2016. However, it is still difficult to provide in situ SSS and biological variables at synoptic scales with frequent coverage owing to the lack of ship-based measurements.

Traditional in-situ measurements of SSS have been improved by the recent increase in the number of observing ships and the development of Argo floats. Owing to uneven and limited sampling coverage, in situ SSS is relatively sparse on both spatial and temporal scales. Although the Argo arrays provide near-global coverage regularly, the ECS is a river-dominated marginal sea shallower than 200 m, which is not observed in the Argo floats. Measuring SSS from space is an alternative to tracking the spatial and temporal variability of SSS governed by freshwater outflow from rivers and routine monitoring over marginal seas. With the advent of remote-sensing technology, SSS has been remotely sensed from recently launched satellite missions, such as NASA's AQUARIUS, ESA's Soil Moisture and Ocean

Salinity (SMOS), and NASA's Soil Moisture Active Passive (SMAP). Considering that SSS is a key parameter in tracking physical and biological processes, mapping SSS more precisely with satellite observations and combining it with other satellite measurements will enable the monitoring of environmental variables in river-dominated marginal seas. In this study, we combined recently available SSS products from the SMAP mission with other remote sensing measurements to investigate the impact of river-discharged freshwater on surface environmental variables. This study focused on how freshwater discharged from Changjiang affects the physical and biological responses and oceanic uptake of CO_2 in the northern ECS shelf. We expect that the ability to more precisely evaluate river-induced environmental changes will be further improved by utilizing completely independent satellite observations.

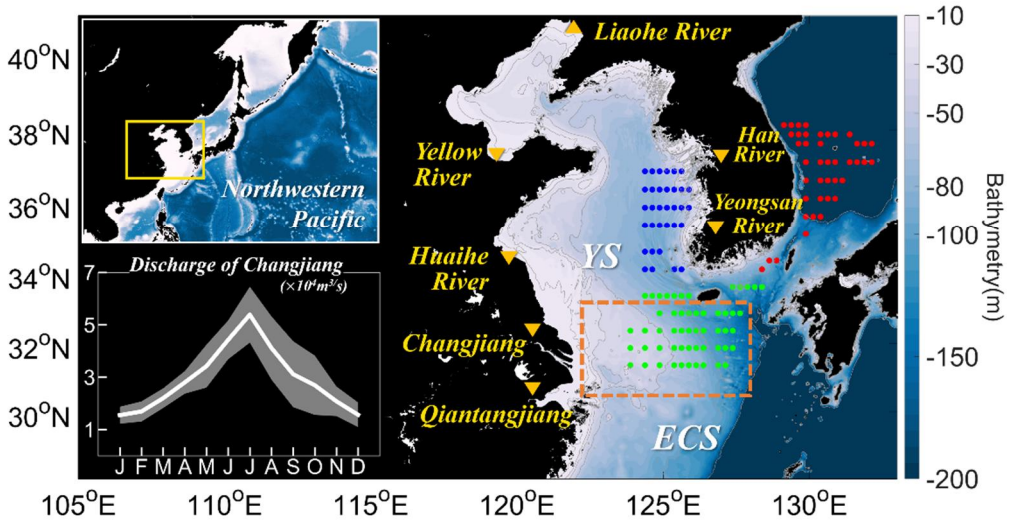

Figure 1. Geographic map of the East Asian marginal seas (inserted map) and enlarged map of the Yellow Sea (YS) and East China Sea (ECS) with bathymetry (meter). Hydrographic stations provided by the Korea Oceanographic Data Center of the National Institute of Fisheries Science (NIFS) are marked by blue, red and green dots for the western sea of the Korean Peninsula (WSK), eastern sea of the Korean Peninsula (ESK), and northern East China Sea (NECS), respectively. The orange dashed box indicates the northern ECS region where the environmental variables are averaged in section 5. Seven rivers are marked by yellow triangle with their names. The insert time series indicates the annual discharge of the Changjiang, which contributes about 90% of the whole river discharge into the ECS. The Changjiang discharge was monthly averaged from 2015–2022, and the shaded area denotes one standard deviation around the mean.

2. Data and method

2.1 Datasets

The SMAP SSS L3 version 4 and 5 datasets generated produced by Remote Sensing Systems (RSS, Entekhabi et al., 2010; Meissner, 2018) were used in this study to identify spatial and temporal SSS variability. Since the RSS version 4 is available from March 2015 to December 2021, we extended the SSS data length to December 2022 using the RSS version 5 product (Table. 1). The L3 products are global and daily dataset using 8-day running mean on a spatial grid resolution of 0.25° and monthly means were obtained from the gridded daily data. Because there was gap in the SMAP product from June to July 2019 owing to a spacecraft issue (Reichle et al., 2022), we used the climatological monthly means over the available period of the dataset to fill the data gap. Remote sensing SSS measurements, which are based on L-band radiometer sensitivity, are known to be influenced by radio frequency interference (RFI) and land contamination (Kolodziejczyk et al., 2016; González-Gambau et al., 2017). Recently, the L-band microwave sensor has been improved through many efforts in establishing the approaches (Le Vine, 2019). SMAP includes additional special hardware and software systems that enable to detect RFI and filter it out (Le Vine, 2019). Although RFI and land contamination remain uncertain, recent studies on SSS remote sensing have demonstrated the possibility of monitoring regional marginal seas up to approximately 40 km from the coast (Grodsky et al., 2019; Vinogradova et al., 2019; Akhil et al., 2020; Menezes, 2020; Fournier and Lee, 2021). For example, SMAP has improved the understanding of SSS variability in the coastal regions, which are predominantly affected by the river plume (Akhil et al., 2020; Menezes. 2020; Fournier and Lee. 2021). SMAP can also stably capture SSS signals in regions such as semi-enclosed areas (Grodsky et al., 2019; Menezes et al., 2020).

To validation of satellite SSS measurements, we compare the SMAP SSS with in situ

data measured by shipboard CTD casts provided by the Korea Oceanographic Data Center of the National Institute of Fisheries Science (NIFS). Since 1961, the NIFS has regularly measured various oceanic variables around the Korean Peninsula at bimonthly interval. The serial shipboard survey provides in situ hydrographic and other variables profiles, including water temperature, salinity, and dissolved oxygen, at hydrographic stations (Fig. 1). Total of 129 hydrographic stations are used in comparison with SMAP SSS. After the data nearer than ~40 km from the coast were removed, the in-situ data are matched with the nearest SMAP grid point.

To identify the impact of SSS on SST warming response during study period, three SST products based on satellite-observation were used: the Operational Sea Surface Temperature and Ice Analysis (OSTIA), The NOAA Optimum Interpolation 1/4-degree daily Sea Surface Temperature Analysis Version 2 (OISST), and the Group for High Resolution Sea Surface Temperature (GHRSST) (Table 1). OSTIA was generated by the UK Met Office. OSTIA analysis combines in situ data from ships and buoys, passive microwave satellite SST measurements, and infrared instruments such as the multichannel AVHRR (Donlon et al., 2012). This SST product has been providing daily, high spatial resolution (0.05°), global analysis since 2006. The monthly SST averaged from the gridded daily data was used from 2015 to 2022 in this study. NOAA OISST, which uses advanced, high-resolution radiometer data is one of the most widely used SST product in various fields and has a spatial resolution of 0.25° and has generated daily temporal resolution for the longest period from 1981 to the present day. This product includes a large-scale adjustment of satellite biases based on in situ from ships and buoys (Reynolds et al., 2007). The monthly mean of SST was used from 2015 to 2022. Lastly, GHRSST Level 4 SST analysis provided by JPL Physical Oceanography DAAC was also used to compare with other two SST products. Spatial resolution of the data is 0.01° and the temporal resolution is one day with global coverage (Chin et al., 2017).

Ocean color products from the Moderate Resolution Imaging Spectroradiometer/Aqua (MODIS/Aqua) and Visible Infrared Imaging Radiometer Suite (VIIRS) were also utilized to examine the relationship between SSS and *chl-a* concentration. MODIS/Aqua is the primary instrument for NASA's Earth Observing System, and the *chl-a* concentration is derived from NASA's ocean color satellite sensors (Moore et al., 2009). MODIS/Aqua provides a spatial resolution of 0.04° and a monthly temporal resolution for the period 2015-2022. MODIS/Aqua has 36 spectral channels. The primary bands for ocean color measurements of them are nine channels covering the 400-900 nm spectrum, and the *chl-a* concentration is derived from empirical algorithms using reflectance ratios (Franz et al., 2005). Similar to MODIS/Aqua, VIIRS is a multispectral imaging sensor capable of obtaining global thermal data, and *chl-a* concentration is measured through three imaging bands at the wavelengths of 638, 862, and 1600nm (Wang et al., 2018). VIIRS provides various oceanic products, including *chl-a* concentration, on a spatial resolution of 0.04° from 2015-2022 (Wang et al., 2014; Wang et al., 2016). Monthly *chl-a* concentrations products for both MODIS/Aqua and VIIRS were used. Satellite altimetry products from 1993 to 2020 were used in this study.

Table 1. The main features of satellite products of SSS, SST, and *chl-a* concentration.

Variables	Satellite Data (Data download link)	Resolution		Period used	Time period
		Spatial	Temporal		
Sea Surface Salinity (**SSS**)	**SMAP** RSS SMAP Level 3 Image 8-Day Running Mean V4.0 Validated Dataset (https://podaac.jpl.nasa.gov/dataset/SMAP_RSS_L3_SSS_SMI_8DAY-RUNNINGMEAN_V4)	0.25º x 0.25º	daily	2015.03 ~ 2021.12 (except period (non-data) : 2019.06 ~ 07)	2015.03 ~ 2019.05 2019.08 ~ 2021.12
	SMAP RSS SMAP Level 3 Image 8-Day Running Mean V5.0 Validated Dataset (https://podaac.jpl.nasa.gov/dataset/SMAP_RSS_L3_SSS_SMI_8DAY-RUNNINGMEAN_V5)	0.25º x 0.25º	daily	2022.01 ~ 2022.12	2022.01 ~ Present
Sea Surface Temperature (**SST**)	**OSTIA** The Operational Sea Surface Temperature and Ice Analysis (https://podaac.jpl.nasa.gov/dataset/OSTIA-UKMO-L4-GLOB-v2.0#)	0.05º x 0.05º	daily	2015 ~ 2022 (only August)	2006.12.31 ~ Present
	OISST.v2 AVHRR NOAA optimum Interpolation ¼ Degree Daily Sea Surface Temperature Analysis, Version 2 (https://www.ncei.noaa.gov/products/optimum-interpolation-sst)	0.25º x 0.25º	daily		1981.09 ~ Present
	GHRSST L4 GHRSST Level 4 MUR Global Foundation Sea Surface Temperature Analysis (v4.1) (MUR-JPL-L4-GLOB-v4.1) (https://podaac.jpl.nasa.gov/dataset/MUR-JPL-L4-GLOB-v4.1#)	0.01º x 0.01º	daily		2022.05.31 ~ Present
Chlorophyll-a concentration (***chl-a concentration***)	**MODIS - Aqua** Moderate Resolution Imaging Spectroradiometer (http://apdrc.soest.hawaii.edu/erddap/griddap/hawaii_soest_69ee_7d0d_74e6.html)	0.04º x 0.04º	Monthly, Daily	2015 ~ 2022 (only August)	2002.07 ~ 2023.02
	VIIRS NASA/NOAA The Visible Infrared Imaging Radiometer Suite (https://polarwatch.noaa.gov/erddap/griddap/erdVH2018chlamday.html)	0.04º x 0.04º	Monthly, Weekly, Daily	2015 ~ 2022 (only August)	2012.01 ~ 2022.12 2022.01 ~ Present (only Daily)

2.2 Method

The accuracy of the satellite SSS is influenced by sea-surface roughness caused by wind and precipitation conditions as well as SST condition (Grodsky et al., 2018; Qin et al., 2020). Recently, Qin et al. (2020) proposed a multiple linear regression (MLR) method adopting wind speed, precipitation, and SST data to correct the bias between SMAP and in situ SSS. In this study, the bias, defined as the SMAP minus in situ SSS, is corrected in the same way as the following of Qin et al. (2020).

$$\hat{b} = a_0 + a_1 \times SST + a_2 \times WS + a_3 \times P + \varepsilon \quad (1)$$

where a_0 is the intercept, a_1, a_2, a_3 are the regression coefficients with respect to the SST, wind speed (WS), and precipitation (P), respectively, and ε is the error. The variables used in this regression model were obtained from ECMWF ERA5 reanalysis monthly dataset (Hersbach et al., 2023). The original SMAP SSS is regionally corrected by subtracting the biases ($\hat{b}$) obtained from the linear regression model as the following equation.

$$Bias\ Corrected\ SSS = Original\ SSS - \hat{b} \quad (2)$$

The sea surface pCO_2 plays an important role in the ocean carbonate system and the global carbon cycle. They also mainly controlled by physical and biological processes, which are related to oceanic environments, such as SST, SSS and *chl-a* concentration (Takahashi et al., 2002; Sarma et al., 2006). Nevertheless, in situ data of the surface pCO_2 are insufficient on the global ocean scale, and even more lack in the marginal sea. Therefore, several previous studies have been attempted to estimate the surface pCO_2 using from various methods such as MLR, MNR, and machine learning with satellite data, in situ, and climatological observation data (Chen et al., 2016; Bai et al., 2015; Chen et al., 2019; Liu et al., 2023). We here estimate the sea surface pCO_2 by combining SMAP SSS with satellite-based SST and *chl-a* concentration, based on multiple nonlinear regression (MNR) method which was successfully applied to the ECS shelf region by Liu et al. (2023). They have shown that the best performance was obtained when SST, SSS, *chl-a* concentration, Julian Day (JD),

longitude, and latitude were given as the independent parameters. Therefore, the same MNR approach and variables as in Liu et al. (2023) was applied in our estimation as follows.

$$
\begin{aligned}
pCO_2 = {} & 1614.69x_1 + 203.92x_2 - 260.69x_3 - 9793.60.x_4 + 98.93x_5 - 1364.95x_6 + 3.23x_1x_2 \\
& + 0.89x_1x_3 + 7.53x_1x_4 - 13.99x_1x_5 + 0.09x_1x_6 + 0.91x_2x_3 - 29.68x_2x_4 - 4.86x_2x_5 \\
& + 8.33x_2x_6 - 14.49x_3x_4 - 0.15x_3x_5 + 7.28x_3x_6 + 86.04x_4x_5 + 4.78x_4x_6 + 8.17x_5x_6 \\
& - 0.24x_1^2 + 1.27x_2^2 + 0.13x_3^2 - 15.01x_4^2 + 0.07x_5^2 + 1.61x_6^2 + 2.49(\text{year}-2006), \\
& \gamma = 255
\end{aligned}
\tag{3}
$$

where, x_1 = SST, x_2 = SSS, x_3 = *chl-a* concentration, $x_4 = \cos(2\pi(\text{JD}- \gamma)/365)$, x_5 = longitude, and x_6 = latitude. JD indicates Julian day, which is normalized to represent the seasonal cycle. A detailed description of the parameters is described in Liu et al. (2023).

To investigate the spatiotemporal behavior of freshwater discharged from Changjiang, a cyclostationary empirical orthogonal function (CSEOF) analysis was performed on the bias-corrected monthly SMAP SSS gridded data (Kim and North, 1997). In recent years, CSEOF has been widely used to extract internal variability in a wide range of climate signals (Yeo and Kim, 2015; Zhi et al., 2020; Scanlon et al., 2022). In CSEOF analysis, space-time data (T(r, t)) are decomposed into cyclostationary loading vectors (LV_n(r, t)), and their corresponding principal component (PC) time series (PC_n(t))

$$T(r,t) = \sum_n LV_n(r,t)PC_n(t) \tag{4}$$

where, r, t, and n denote the space, time, and the mode number, respectively (Kim and North, 1997; Yeo and Kim, 2013). CSEOF loading vectors are periodic in time:

$$LV_n(r,t) = LV_n(r,t+d) \tag{5}$$

where d is a specific period, called the “nested period”. Because the dominant mode of SSS in study area is seasonal variation, the nested period was set to be 12 months. These equations above indicate that each LV represents a set of spatial patterns that evolve within

the nested period, and the periodic LV's amplitude is changed by the PC time series. In other words, in CSEOF analysis the physical variation during the nested period is captured in the resulting the LV (i.e., spatial patterns), and the corresponding PC time series depicts the amplitude of the variation of the physical process (Yeo and Kim, 2013). Unlike EOF analysis, the CSEOF LVs enable to capture the physical evolution of an inherent physical process in a given dataset. Further details on the CSEOF decomposition are provided by Kim et al. (2015).

3. Validation and Correction for SMAP SSS

Although advances in remote sensing technologies have greatly improved the capability of SSS measurements from space, SSS retrieval in marginal seas is still challenging due to water temperature and land effects (Dinnat et al; 2019; Le vine and Dinnat; Reul et al., 2020). Therefore, SSS retrieved from SMAP is needed to validate against in situ measurements and further bias corrected using reanalysis products. The data nearer than ~ 40 km from the coasts were removed from the validation to minimize the influence of land effects (Vinogradova et al., 2019). Because several water masses were distributed in the study area, we grouped three regions: the western sea of Korean peninsula (WSK), the eastern sea of Korean peninsula (ESK), and the northern East China Sea (NECS).

Fig. 2 presented the validation results based on seven years of SMAP SSS in the three regions. Overall, SMAP SSS was in good agreement with the in-situ measurements for all regions, and the correlation coefficient, bias, and RMSE were 0.76, -0.64, and 0.73, respectively (Fig. 2). For all regions, SMAP SSS shows a conspicuous freshening bias, ranging from -0.75 to -0.42. The lowest bias occurred in the NECS with warmer SST throughout the year, and SMAP SSS in the NECS had a high correlation of 0.93 with in situ data. The negative SMAP biases for all regions had a distinct seasonal variability with high-

frequency variability, increasing in the cold season and decreasing warm season (Fig. 3). The relatively strong freshening biases of SMAP during cold season were consistent with previous studies that have identified an inherent retrieval bias related to seasonal changes in ocean surface conditions (Tang et al., 2017; Boutin et al., 2018; Grodsky et al., 2018; Dinnat et al., 2019; Qin et al., 2020). To identify variables affecting the seasonal bias, we examined the relationship between SST, wind speed and rainfall over the study areas. The time series of the regional monthly average SSS bias, SST, and wind speed was presented in Fig. 4. The correlation between the SSS bias and the variables had the highest correlation of 0.60 for SST, followed by -0.35 for wind speed, and 0.34 for rainfall (Fig. 6 and Table. 2). Regionally, the correlation coefficients between SMAP SSS and SST were 0.72 in WSK, 0.73 in ESK, and 0.56 for NECS (Fig. 5 and Table. 2). These results suggest that the bias of SMAP SSS is predominantly affected by seasonal variability of SST, but it has relatively weak correlation with wind speed and rainfall. In particular, the correlation between the bias and SST is relatively higher in WSK and ESK, where the SSTs drop below 5°C in winter. The bias in both two regions have stronger negative values in cold season, indicating that the seasonal bias in the study region is related to the decrease in the sensitivity of the SMAP microwave sensor to cold water (Grodsky et al., 2018).

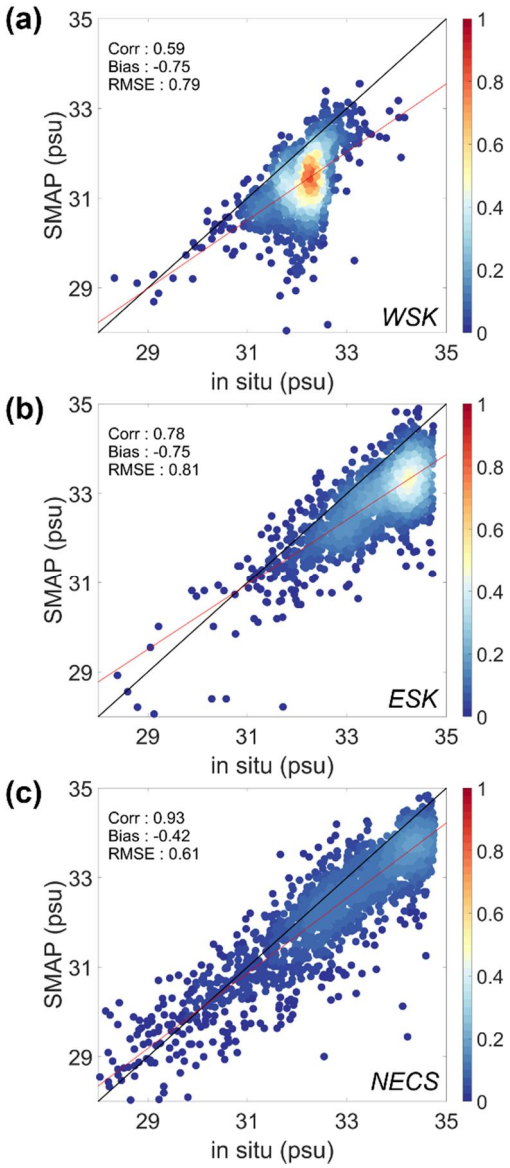

Figure 2. Scatter plots of monthly SMAP SSS versus in situ SSS data from 2015 to 2021 for (a) the western sea of Korean Peninsula (WSK), (b) eastern sea of Korean Peninsula (ESK), and (c) northern ECS (NECS).

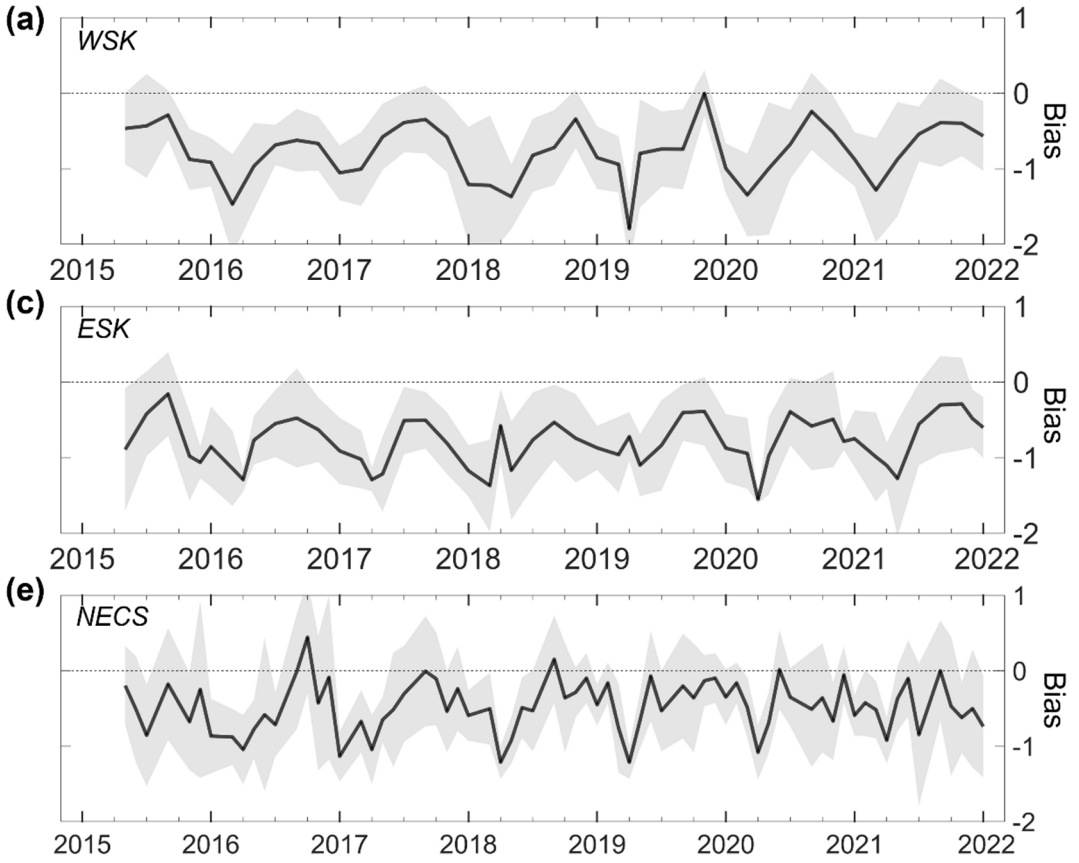

Figure 3. Time series of area-averaged bias between SMAP and in situ SSS for (a) the western sea of Korean Peninsula (WSK), (b) eastern sea of Korean Peninsula (ESK), and (c) northern ECS (NECS). The shaded areas denote one standard deviation around the mean.

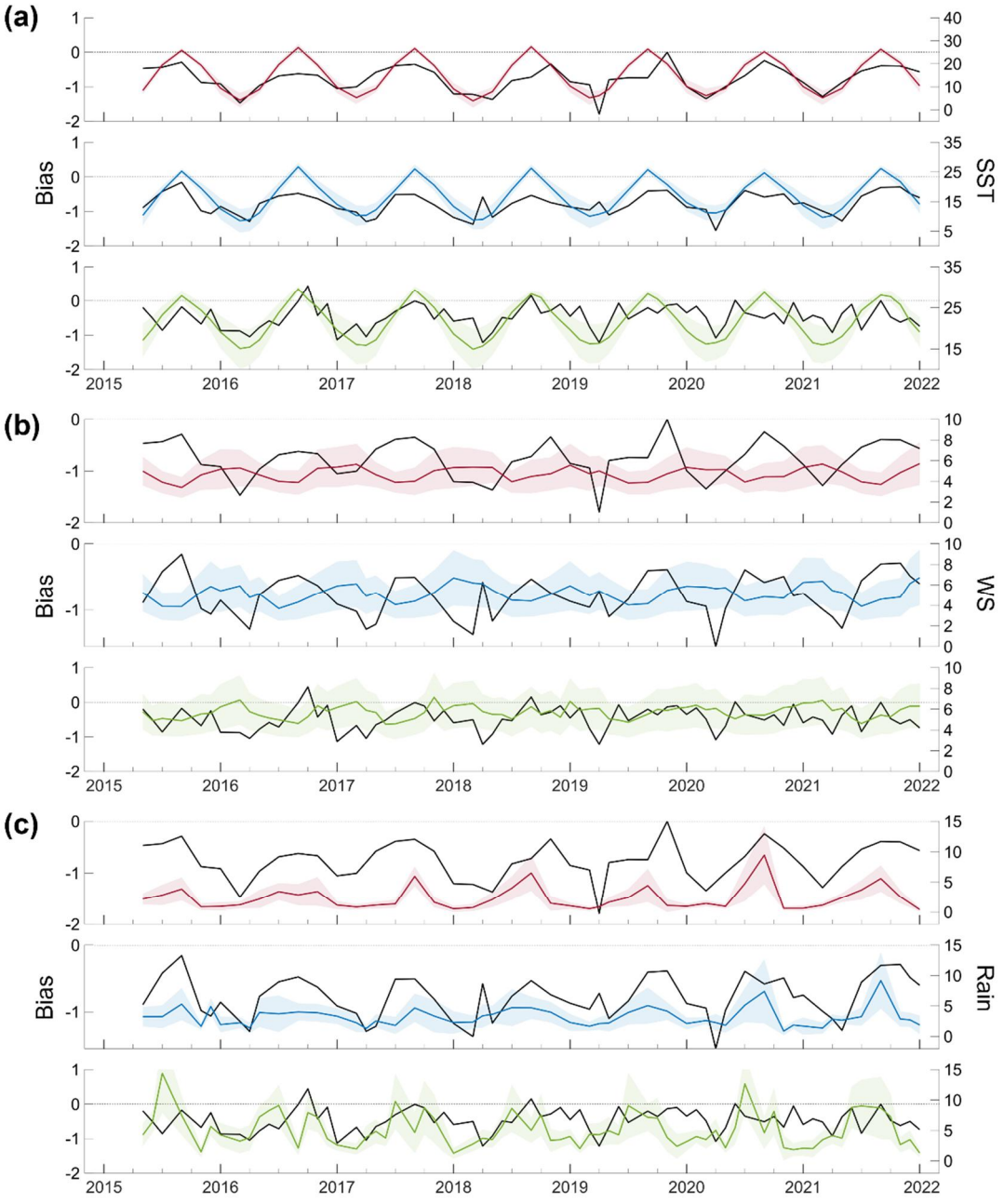

Figure 4. Comparisons of SMAP SSS bias with (a) sea surface temperature (SST), (b) wind speed (WS), and (c) rainfall averaged for the WSK (red), ESK (blue), and NECS (green) from 2015 to 2021. The shaded area denotes one standard deviation around the mean of each data.

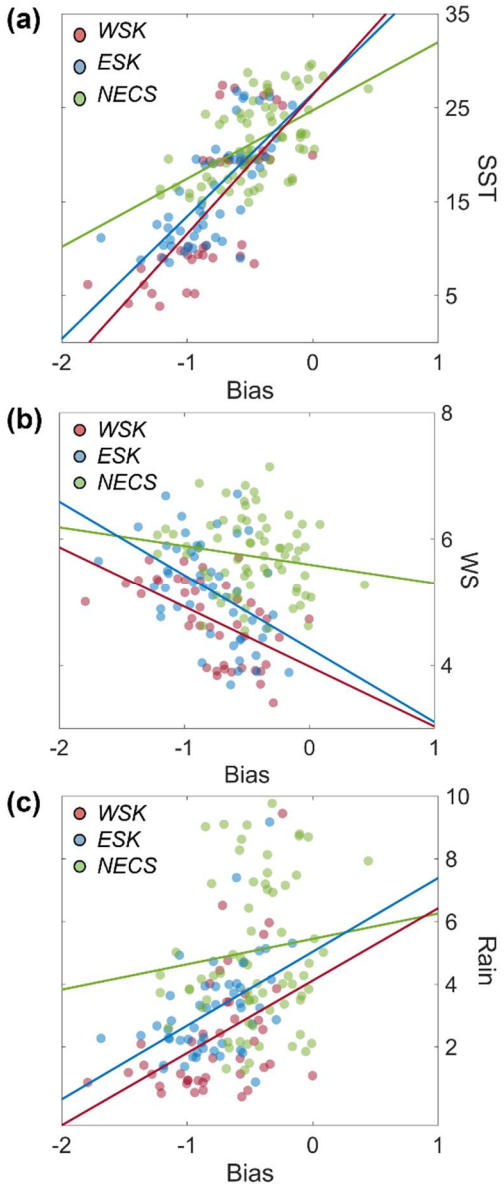

Figure 5. Scatter plot of monthly area-averaged SSS bias (black) and (a) SST, (b) wind speed, and (c) rainfall for the WSK (red), ESK (blue), and NECS (green) from 2015 to 2021.

Table 2. Summary of the correlation coefficient between the SMAP SSS bias and SST, wind speed, and rainfall for each region (WSK, ESK, and NECS) and all regions from 2015 to

Regions	SST	WS	Rain
WSK	0.72**	-0.55**	0.44**
ESK	0.76**	-0.49**	0.50**
NECS	0.55**	-0.19	0.11
All regions	0.61**	-0.35**	0.37**

**Correlations (R) were statistically significant ($P < 0.01$).

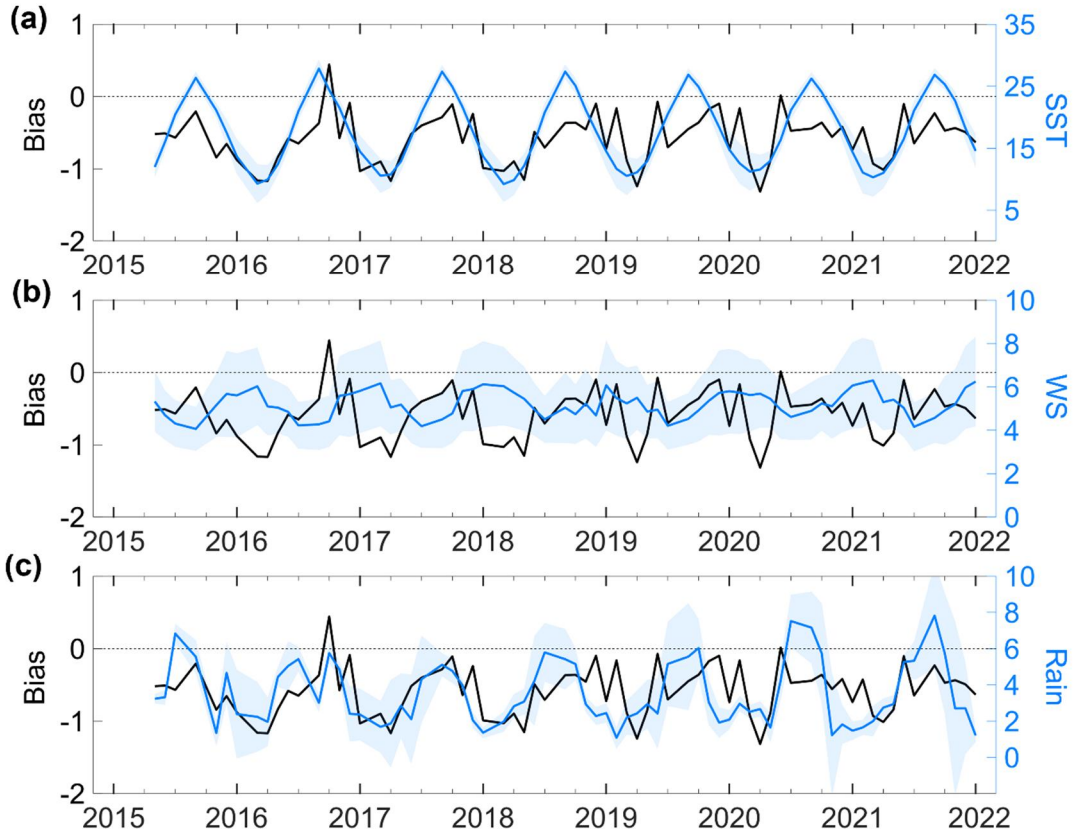

Figure 6. Comparisons of SMAP SSS bias with (a) sea surface temperature (SST), (b) wind speed (WS), and (c) rainfall averaged for all regions from 2015 to 2021. The shaded area denotes one standard deviation around the mean of each data.

Based on the validation results mentioned above, the seasonal bias of SMAP SSS was corrected by conducting MLR with SST, wind speed, and rainfall. The results are shown in Figs. 7 and 8, which present the SMAP SSS bias explained by MLR model and the bias-corrected SSS results. The MLR model generally explained the seasonal variability of the SMAP SSS bias over the period of 2015–2022 (Fig. 7), indicating that the variables used in the regression model captured well the seasonal dependence of the SMAP bias. The bias-corrected SSS improved the RMSE and bias by more than 0.3 and 0.6 for the WSK and the ESK in which the correlation between the bias and the SST was high (Figs. 8a and b). Although the bias of NECS showed a relatively low correlation with SST, the RMSE and bias of the bias-corrected SSS improve to 0.48 and 0.02, respectively (Fig. 8c). These results suggest that the correction using the MLR method effectively controls the seasonal bias depending on the sensitivity of the SSS measurement radiometer sensor affected by cold temperature. However, this correction method is ineffective in eliminating the high frequency of bias shorter than the seasonal cycle, particularly in the NECS region where high-frequency bias had a larger amplitude. In addition, the high-frequency may be associated with signals interfering with SSS measurement of remote sensing, such as RFI and land contamination. The biases associated with RFI or land contamination require further correction in the future. Nevertheless, bias-corrected SMAP SSS has shown significant reductions in bias and RMSE, suggesting sufficient accuracy for the mechanism analysis of the study regions.

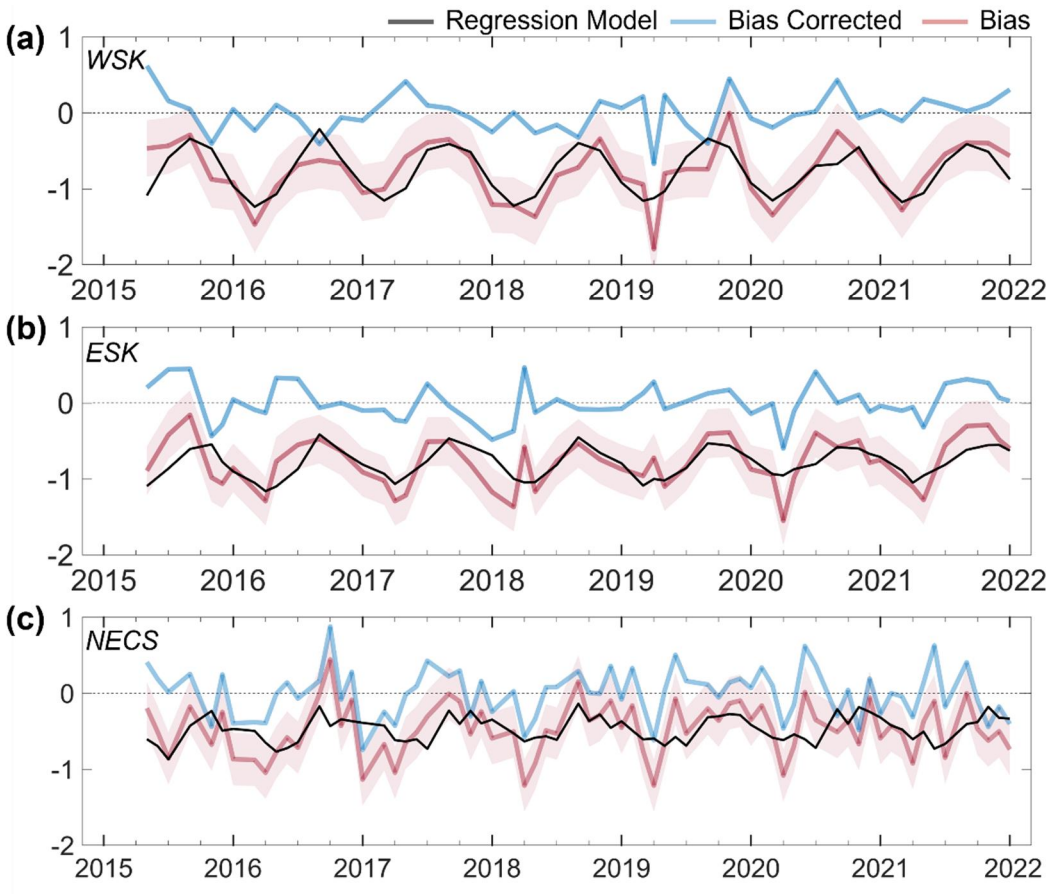

Figure 7. Time series of SMAP SSS bias, estimated bias based on multiple linear regression (MLR) model and corrected bias using the MLR model for (a) WSK, (b) ESK, and (c) NECS from 2015 to 2021. The shaded area denotes one standard deviation around the mean of SMAP bias.

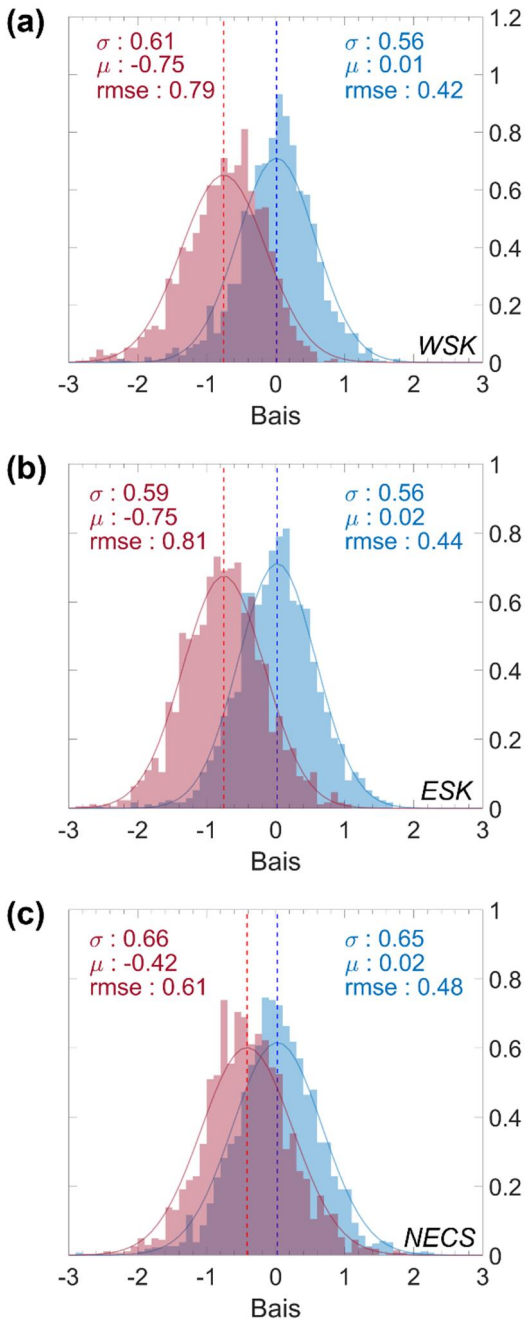

Figure 8. Histogram of the bias-corrected SSS (blue) and the bias SSS (red) at three regions, (a) WSK, (b) ESK, and (c) NECS. σ, μ, and rmse are standard deviation, mean, and root mean square error, respectively.

4. Interannual variability of SSS in the northern ECS

CSEOF analysis was performed to understand the spatiotemporal variability of the corrected SMAP SSS. Each mode of CSEOF analysis provided 12 sequential spatial patterns (LVs) and one PC time series because the nested period was set to 12 months, as shown in Eq (5). Fig. 9 showed the LV and the corresponding PC time series for the first CSEOF mode of SMAP SSS, which explained 79.16% of the total variance. The LV described a robust seasonal cycle in the northern ECS region, with positive anomalies from fall to winter and negative anomalies from spring to summer. The negative anomaly began to appear around the Changjiang mouth in April, and then it spread northeastward to Jeju Island during summer, forming a broad tongue-shaped pattern. The negative anomaly further extended to the ESK during fall and disappeared during winter. This seasonal evolution of SSS was consistent with the northeastward extension of the CDW reported by previous studies (Lie et al., 2003; Moon et al., 2012, 2009), suggesting that the seasonal variation of SSS in the northern ECS depends on the seasonal cycle of freshwater discharged from the Changjiang.

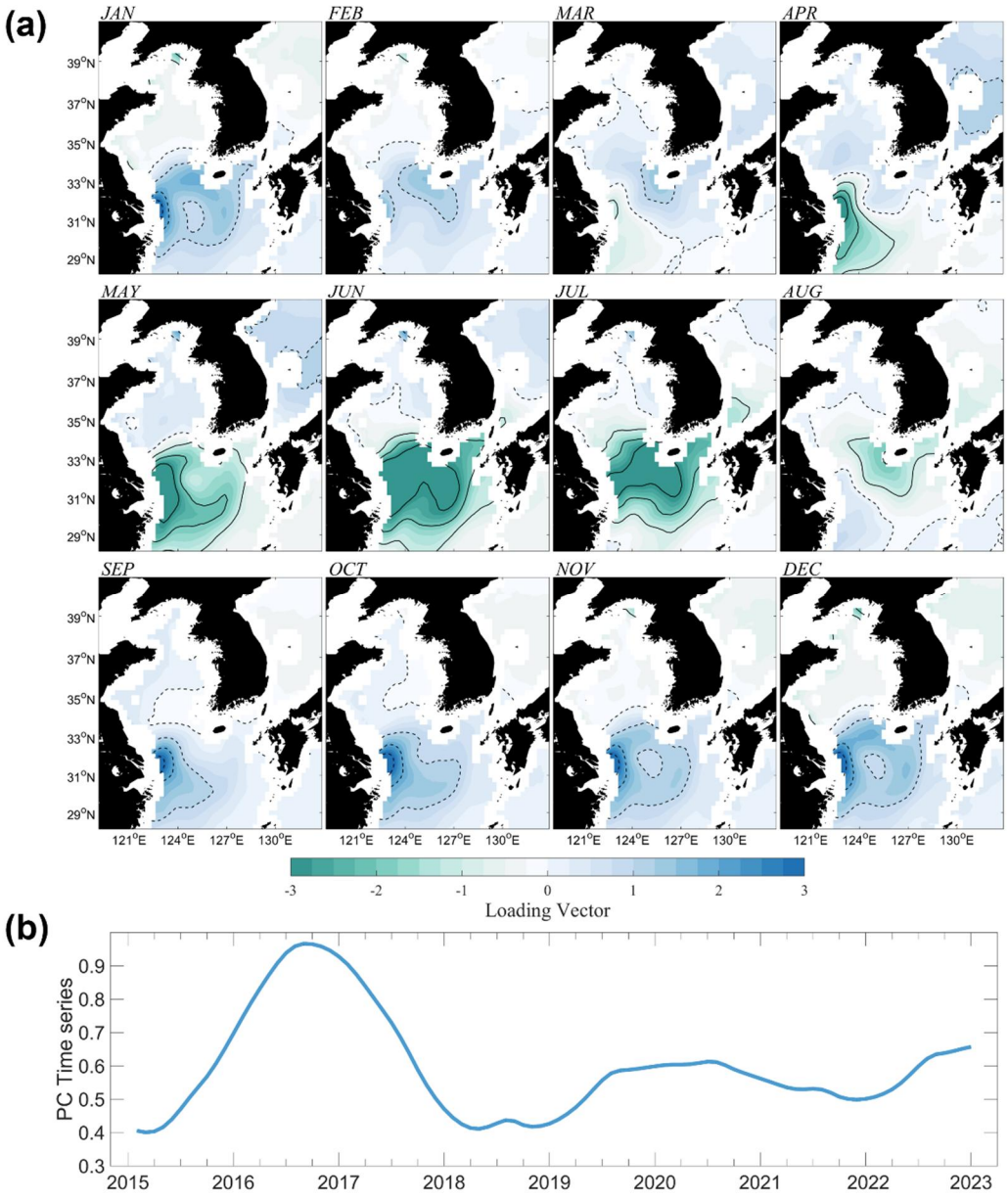

Figure 9. (a) Sequential loading vector (LV) and (b) the corresponding PC time series (solid black line) for the first CSEOF mode of SMAP SSS anomaly from 2015 to 2022. The contour interval is 1.0 with positive and negative values are presented as dashed and solid contours, respectively.

However, the amplitude of seasonal SSS evolution varied from year to year as shown in the PC time series of the first mode, which indicates an interannual SSS variability (Fig. 9b). The PC time series showed a positive value throughout the years, with the maximum in 2016 and the minimum in 2018. This indicates that a significant sea-surface freshening occurred over the northern ECS in the summer of 2016. The comparison between the PC time series and area-averaged SSS in August had an evident inverse correlation, with a significant correlation coefficient of -0.90 (Fig. 10). The negative relationship was clearly evident in the spatial patterns of SSS anomaly (Fig. 11). The SSS negative anomaly was dominated over the study region in 2016, whereas the SSS positive anomaly was predominant in 2018. The contrasting SSS anomaly patterns in 2016 and 2018 explain the maximum and minimum values of the PC time series, respectively (Fig. 11).

The area-averaged SSS in August were also compared with the maximum amount of discharge of the Changjiang in July, as freshwater from the Changjiang took a month to move from the river mouth to the NECS (Fig. 10). As expected, the area-averaged SSS had a significant negative relationship with the discharge of the Changjiang, with a correlation coefficient of -0.85. For example, the negative SSS anomalies were dominant over the northern ECS in 2016 and 2020, when the river discharges were larger than the other years, whereas the positive SSS anomalies prevailed in 2018 (Fig. 11). The interannual mode of CSEOF analysis demonstrated that a distinct seasonal cycle in the northern ECS, and spatiotemporal variability of SSS depends primarily on the interannual variation of discharge of the Changjiang in summer.

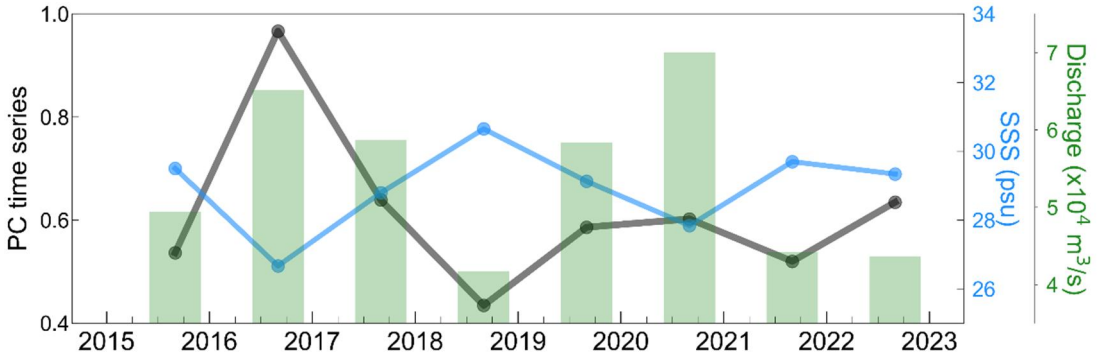

Figure 10. Comparison of corresponding PC time series (solid black line) and the area-averaged SSS (blue line) for the northern ECS (orange dashed box in Fig. 1) in August and the discharge of the Changjiang in July (green bar)

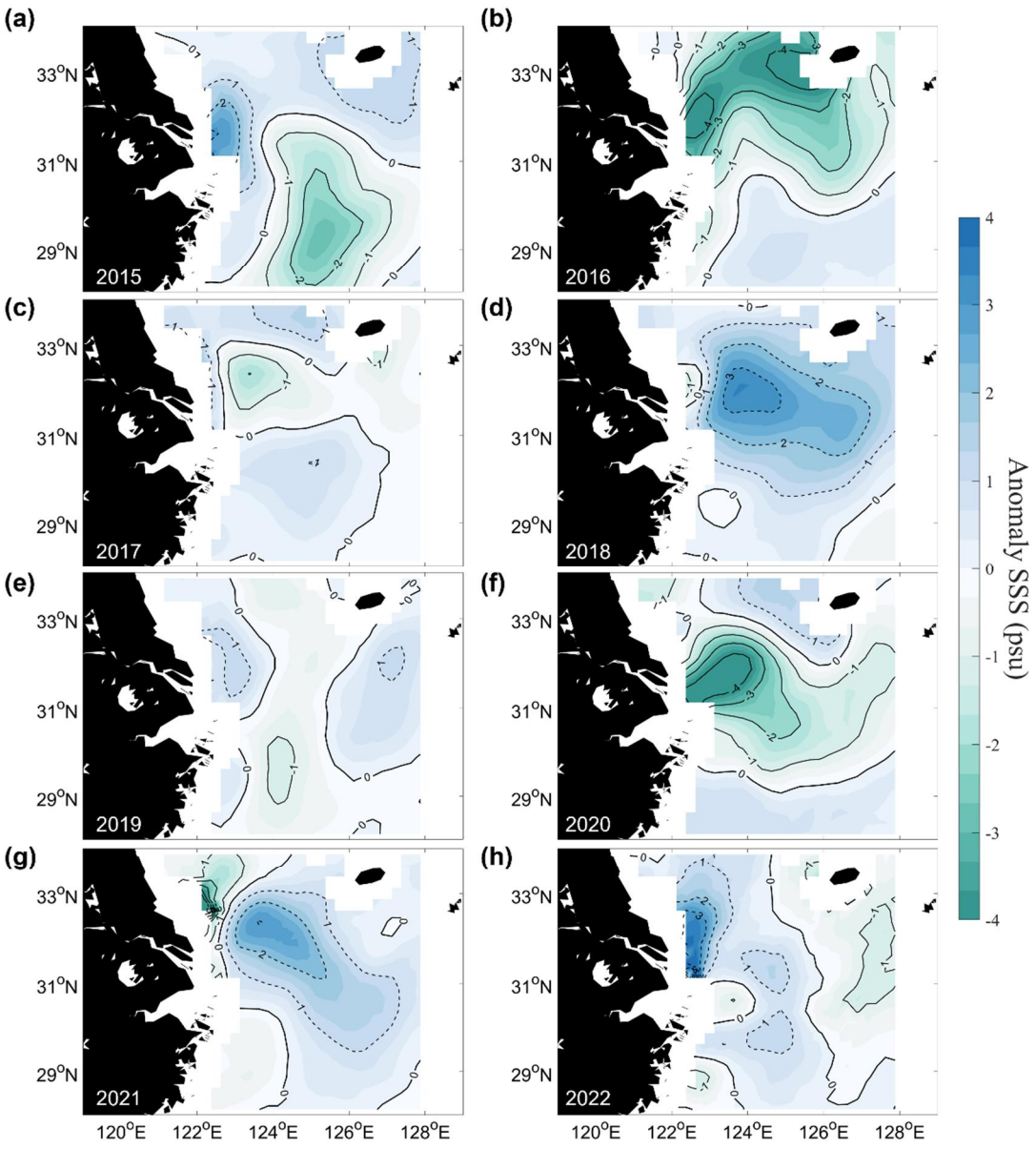

Figure 11. Spatial patterns of SMAP SSS anomaly in August from 2015 to 2022. The contour interval is 1.0 with positive and negative values presented as dashed and solid contours, respectively.

5. Impacts of freshwater on surface ocean environments

5.1 Enhancement of SST warming

In this section, the physical response of SST due to low SSS induced by river-discharged freshwater is analyzed by comparing SMAP SSS and satellite SST anomaly distributions (Fig. 12). The satellite SST anomalies exhibited three warm years in 2016, 2017, and 2022 over the most northern ECS, with the warmest values of more than 2℃ in 2016. Interestingly, these warm anomalies of SST were mostly distributed in the regions where the negative SSS anomalies clearly occurred. In 2016, when negative SSS anomaly was dominant over the northern ECS, the most robust SST warming core was found in the freshening area, which is consistent with the low-salinity core observed in SMAP SSS. Although the negative SSS anomalies in 2017 and 2022 was relatively weaker than in 2016, the evident positive SST anomalies appeared in consistently the low SSS distribution. Because increased solar radiation in summer heats the ocean surface, the spatial pattern of solar radiation anomaly was compared with that of SST and anomaly (Figs. 13). Relatively strong positive anomaly of solar radiation was observed in 2016, 2017, and 2022, which is generally consistent with the years of the enhancement of SST warming. However, the spatial pattern of solar heating showed a distinct difference from the enhanced SST warming pattern. For instance, in 2016, the SST warming core was located in the northern ECS, corresponding to the region with significant surface freshening, whereas the striking solar heating was observed as a zonal band in the northern tip of the ECS. Furthermore, in 2016, wind speed wase comparatively weaker in 2016 than other years, which can help further to strengthen SST warming by weakening ocean surface mixing. The sea surface freshening contributed to the enhancement of SST warming in 2016 which is consistent with the recent result of Moon et al. (2019). They demonstrated that substantial low-salinity water induced

by riverine freshwater in 2016 causes significant SST warming. The freshwater spreading from the Changjiang stratified the surface layer forming a shallow mixed layer, which led to a barrier layer formation. The significant enhancement of barrier layer in turn leads to increased SST warming by restricting heat exchange between the surface and the sub-surface layer over the sea surface freshening areas.

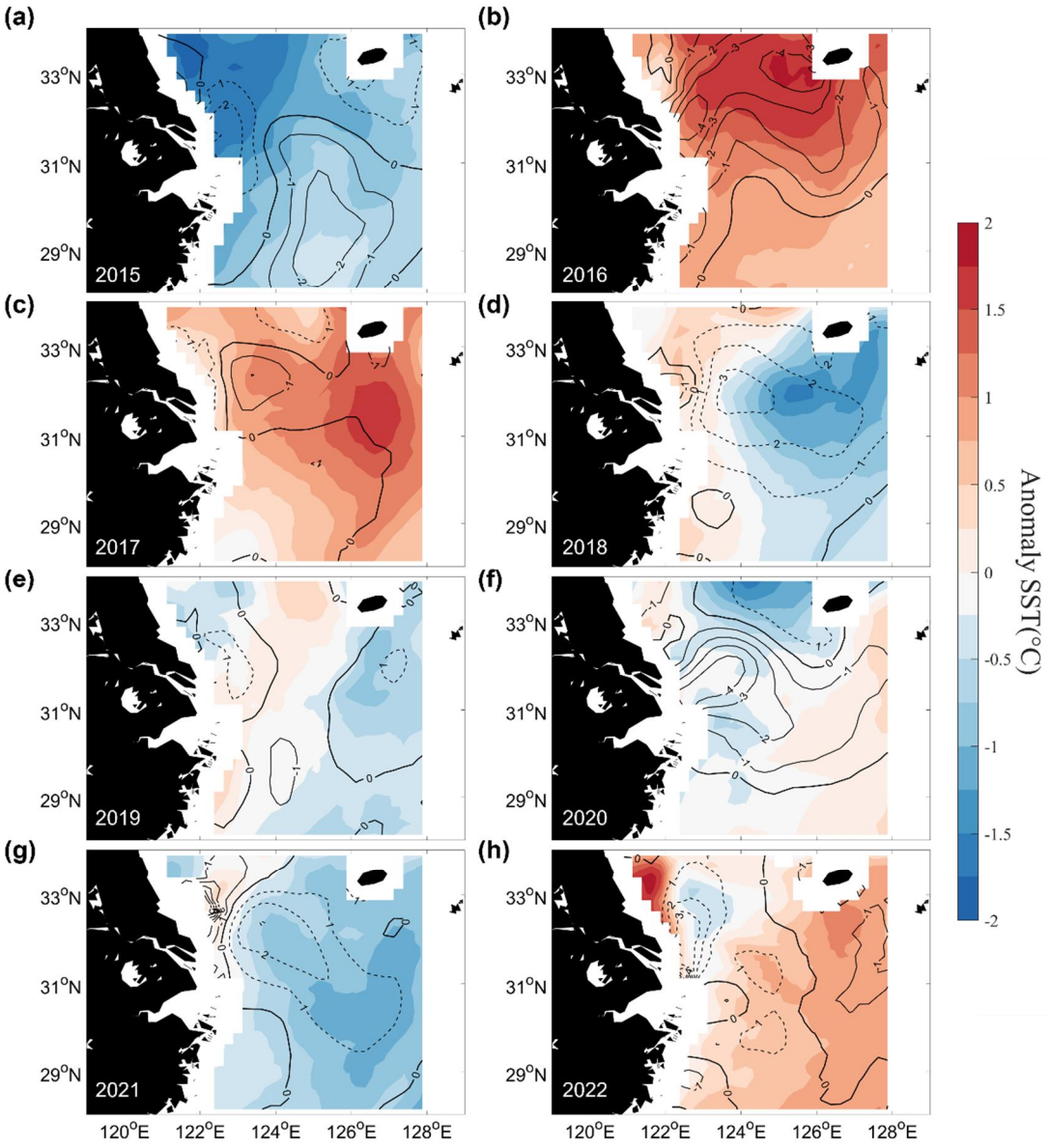

Figure 12. Spatial patterns of SST anomaly (color) averaged for three satellite SST products (OSTIA, OISST, GHRSST) superimposed with SMAP SSS anomaly (contours) in August from 2015 to 2022. The contour interval is 1.0 with positive and negative values presented as dashed and solid contours, respectively.

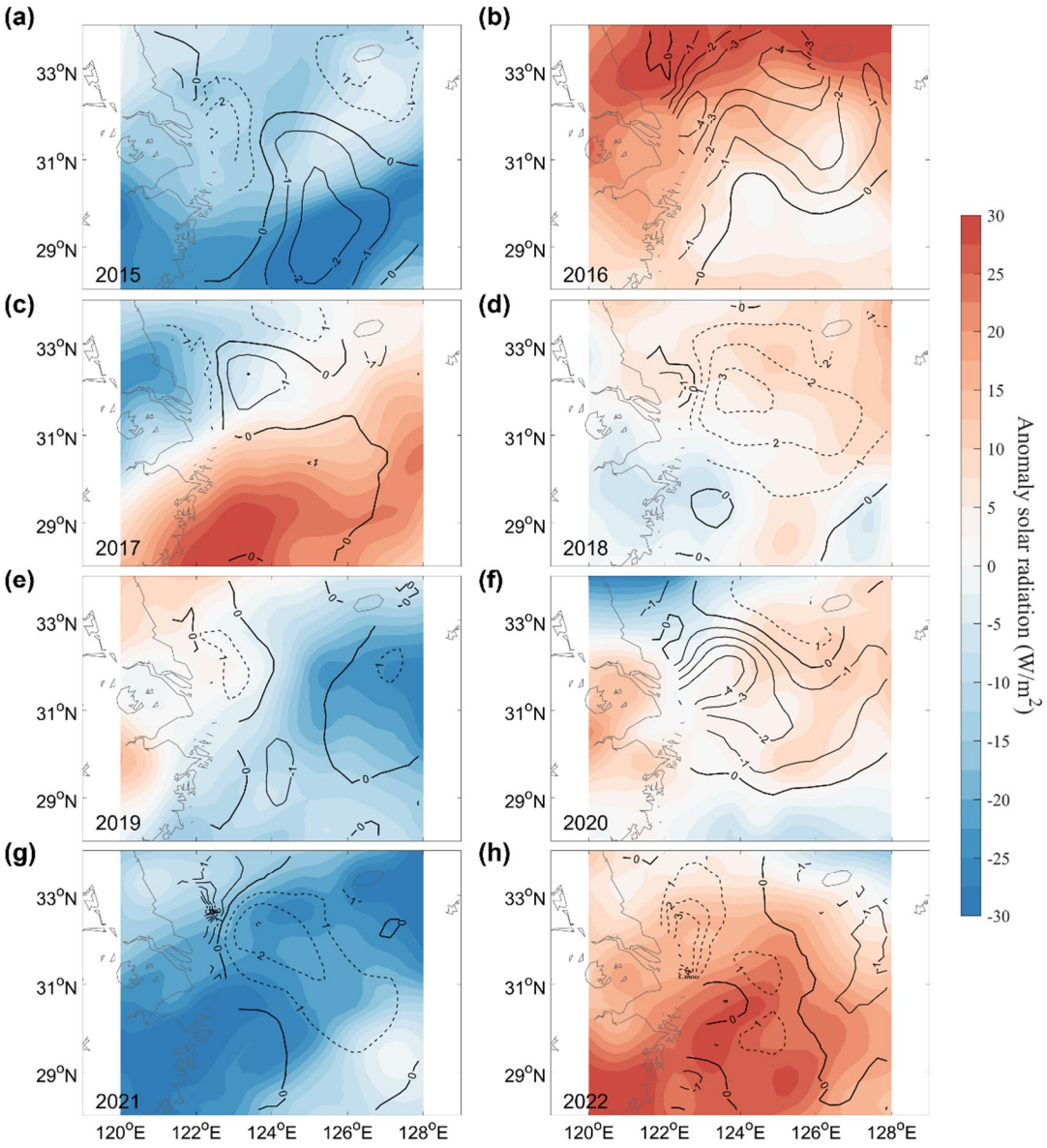

Figure 13. Same as Fig. 7 except for solar radiation anomaly (color) derived from ERA5.

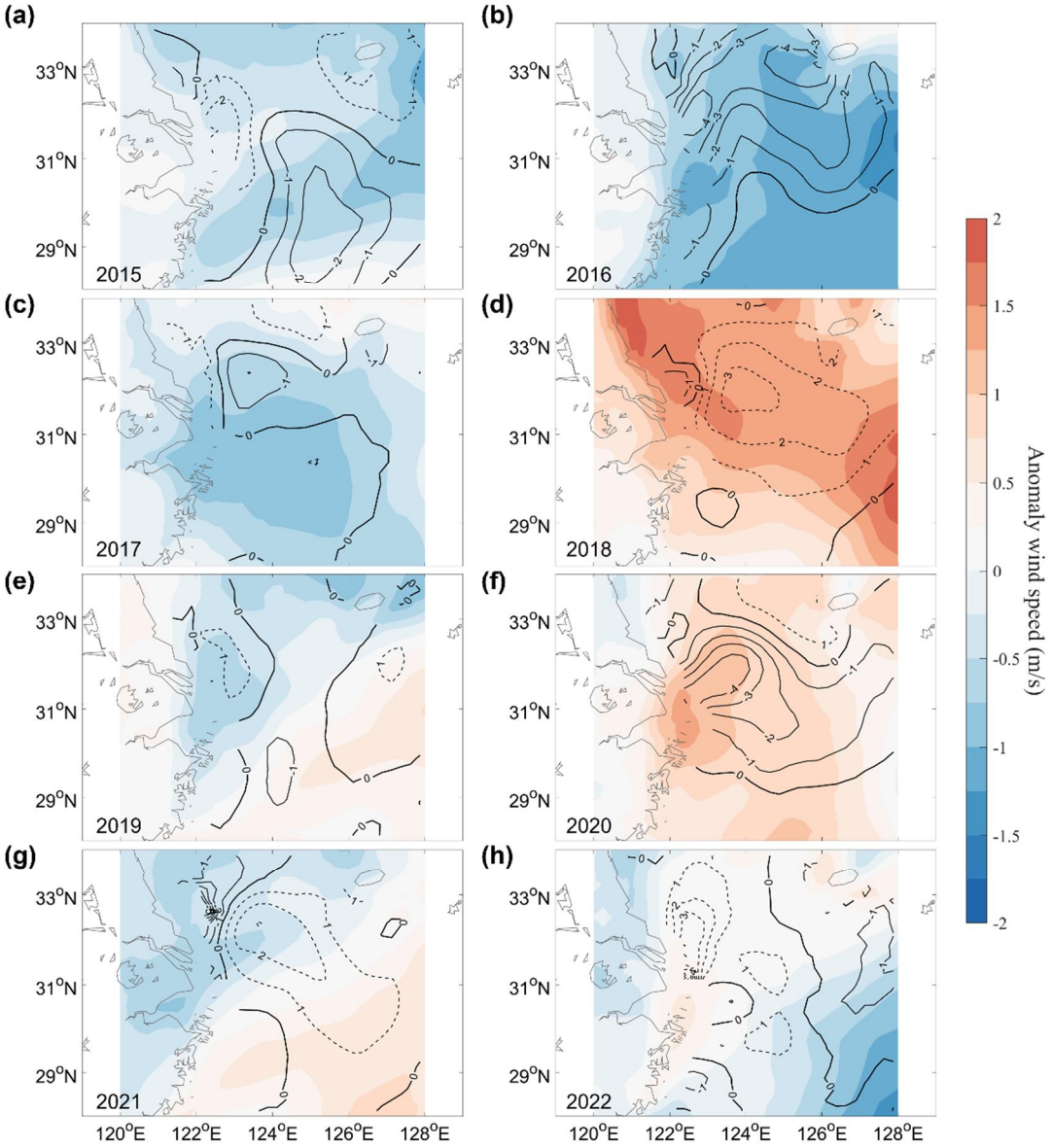

Figure 14. Same as Fig. 12 except for wind speed anomaly (color) derived from ERA5.

Despite the occurrence of abnormally low-salinity in 2015 and 2020, however, SST warming did not appear in these two years, and even coldest in 2015 (Figs. 12a and f). The cold surface water in 2015 was influenced by the lowest solar heating, and consequently the surface freshening did not contribute to the SST warming pattern. Meanwhile, in 2020, even though the low-salinity water extended to the central ECS due to the maximum discharge of the Changjiang, the impact of freshening on SST warming was limited owing to comparatively strong wind-induced sur face mixing, thereby exhibiting no SST warming in the ECS shelf regions (Fig. 14). The connection between SST warming and sea-surface freshening was also clearly evident in Fig. 15, which compares the SMAP SSS with the SST time series derived three different satellite products. All products for SST presented a similar interannual variation over the study period, indicating that the river-influenced SST change is reliable. The ensemble mean SST anomaly showed a significant negative relationship to the SSS anomaly over the period of 2015–2022, with a correlation coefficient of -0.64 (above a significant level of 90%). The comparison of SSS with solar radiation and surface wind variables reveals that under increased solar heating and calm wind conditions, the riverine freshwater can largely enhance the SST warming by trapping heat at the surface layer owing to the restriction of vertical heat exchanges.

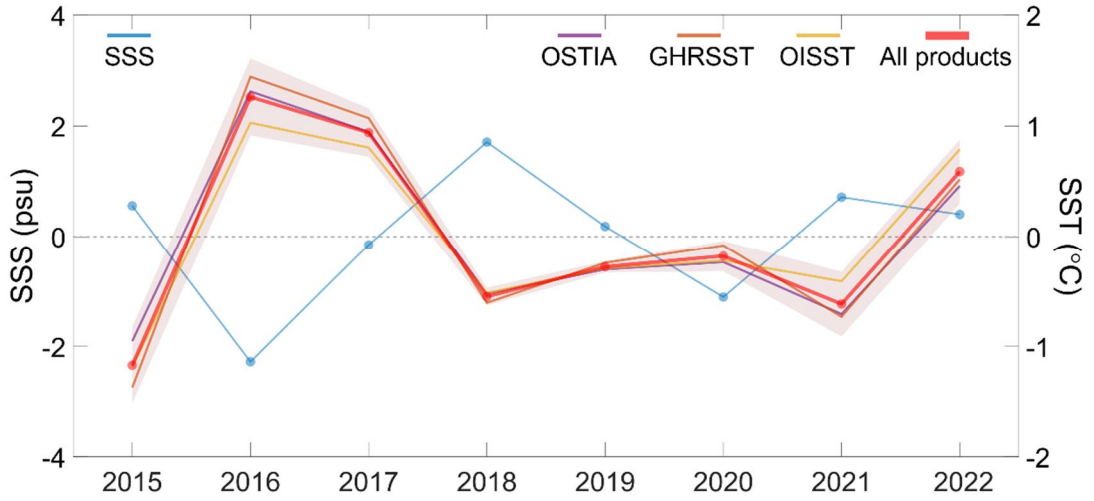

Figure 15. Comparisons of SMAP SSS anomaly with (a) satellite SST anomalies in August from 2015 to 2022. The SST anomalies derived from OSTIA, OISST, and GHRSST products and their mean were shown. Each data was averaged for the northern ECS region (orange dashed box in Fig. 1), and the shaded areas denote two standard deviations around the mean of each data.

5.2 High concentration of *chl-a*

Biological activity is primarily controlled by nutrient levels and physical factors such as temperature and salinity. Since *chl-a* concentration reflects phytoplankton production as it is an essential component for producing energy through photosynthesis in phytoplankton, numerous previous studies have been used *chl-a* concentration as an indicator of primary production (Zhu et al., 2009; Jiang et al., 2015).

To understand the spatiotemporal variability of biological activity associated with riverine freshwater, the spatial distribution of SMAP SSS and *chl-a* concentration derived from MODIS/Aqua were compared (Fig. 16). The high *chl-a* concentration was observed in 2015, 2016, and 2020 over the northern ECS wherein surface freshening was robust. Although the discharge of the Changjiang was relatively low in 2015 (Fig. 10), the higher *chl-a* concentrations were observed in the Changjiang mouth and extended to the central ECS with low salinity anomaly pattern (depicted by less than -2psu). In both 2016 and 2020 when the Changjiang discharges were highest, the positive *chl-a* anomaly was concentrated over the freshening areas, which may be related with the inflow of nutrient-rich freshwater into the ocean from the river discharge (Fig. 16b and f). However, the pattern of positive *chl-a* anomaly showed a distinct difference between the two years. In 2016, high *chl-a* concentration distributed from the river mouth toward the northern ECS with a broad tongue-shaped pattern, which fairly corresponded to the region where substantial surface freshening was intensive. Meanwhile, in 2020, despite the largest amount of discharge of the Changjiang, the high *chl-a* concentration was limited to offshore of the Changjiang mouth and decreased as the salinity increases towards the central ECS (Fig. 16f). The decreased *chl-a* concentration in the central ECS may be associated with wind-induced surface mixing, which can prevent the extension of high *chl-a* concentration (Fig. 14). Furthermore, the intensified SST warming in 2016 may have contributed to maintaining the significant

primary production in the surface layer by restricting surface mixing.

Figure 16. Same as Fig. 12 except for *chl-a* concentration anomaly (color) averaged for two satellite ocean color products (MODIS/Aqua and VIIRS).

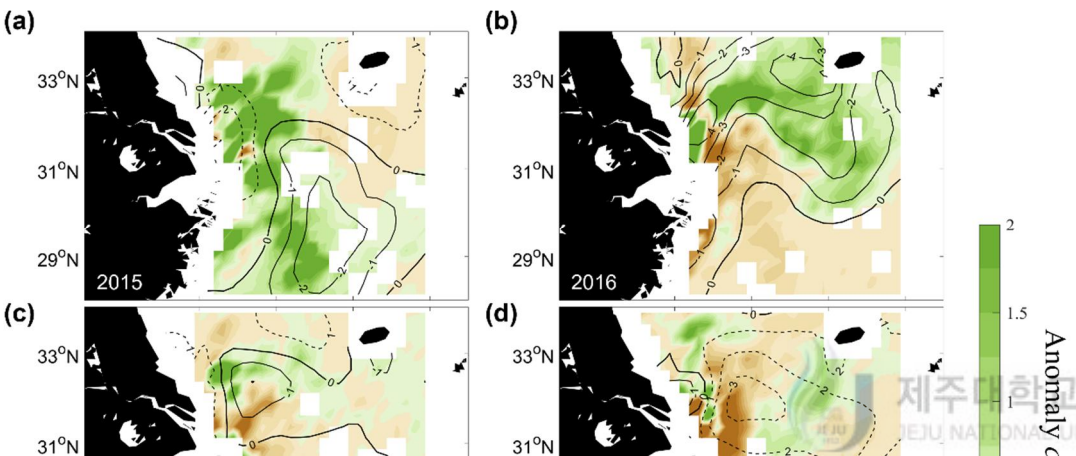

The negative relationship is obviously shown in Fig. 17, which compares interannual variation of SMAP SSS and *chl-a* concentration derived from two satellite datasets, with a correlation coefficient of -0.63 (above a significant level of 90%). These comparisons indicate that the primary production related to high *chl-a* concentration is attributed to large amount of nutrients originated from the Changjiang discharge. As shown in Fig. 16b, the highest concentration of positive *chl-a* was found in 2016, when both the sea-surface freshening and SST warming were intensified over the northern ECS. These spatiotemporal relationship between the SMAP SSS and *chl-a* concentration anomalies suggest that high nutrient levels released from the Changjiang extends to the ECS shelf region along with the buoyant riverine freshwater, resulting in high production of phytoplankton (Fig. 16). In other words, the advection of freshwater discharged from the Changjiang promotes the primary production of phytoplankton biomass in the surface layer, thereby leading to *chl-a* enrichment over the freshening area. In addition to sea-surface freshening, the river-influenced SST warming can help trap the riverine nutrients in the surface layer, contributing to the promotion of biological activity, as clearly shown in the case of 2016.

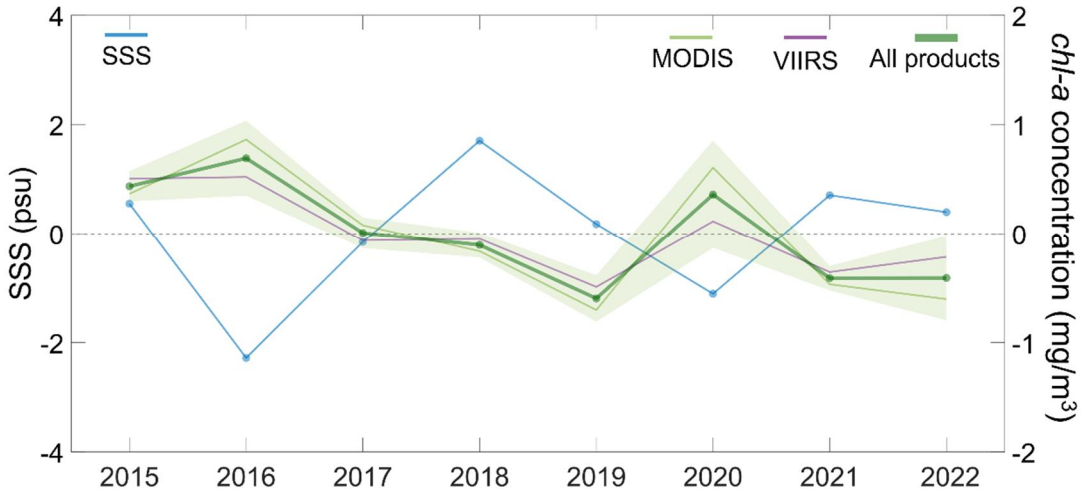

Figure 17. Comparisons of SMAP SSS anomaly with (a) satellite *chl-a* anomalies in August from 2015 to 2022. The *chl-a* anomalies derived from MODIS/Aqua and VIIRS products and their mean were shown. Each data was averaged for the northern ECS region (orange dashed box in Fig. 1), and the shaded areas denote two standard deviations around the mean of each data.

5.3 Reduction of surface pCO_2

The primary production in the sea surface layer consumes oceanic CO_2 that can lead to a reduction of the surface pCO_2. The biological activity as well as thermodynamic effects is a key factor controlling the variability of pCO_2 (Takahashi et al., 2002, 2009; Chou et al., 2017; Liu et al., 2023). In this section, we identified the spatiotemporal variability of pCO_2 and its interconnection with SSS, SST, *chl-a* concentration derived from multiple satellite datasets.

Fig. 18 shows the spatial patterns of estimated pCO_2 anomaly based on the MNR model. The SMAP SSS anomaly was also superimposed to identify the relationship between the surface pCO_2 and SSS. The significant negative pCO_2 anomalies were detected in 2016 and 2020, which corresponded to the years when the river-induced freshening was more intensive. In 2016, decreased pCO_2 pattern was primarily distributed from mouth to over the northern ECS, showing a pattern that obviously matched the spread of low salinity. In addition, this pattern of pCO_2 reduction was consistent with those of high *chl-a* concentration (Fig. 18b). This relationship of pCO_2 with SSS and *chl-a* concentration also appears clearly in 2020, however, the significant low pCO_2 level in 2020 was only detected offshore of the river mouth, and it sharply increases as SSS increased toward the central ECS (Fig. 16). The difference in low pCO_2 level extension between the two years was linked to the pattern of *chl-a* concentration. In 2016, the large amount of nutrients was advected to the northern ECS, forming a broad high production pattern of phytoplankton, which led to the reduction of pCO_2 over the freshening area. On the other hand, the riverine nutrients were only confined offshore of the river mouth due to wind-induced surface mixing effect, resulting in sharp increase in pCO_2 reduction over the central ECS.

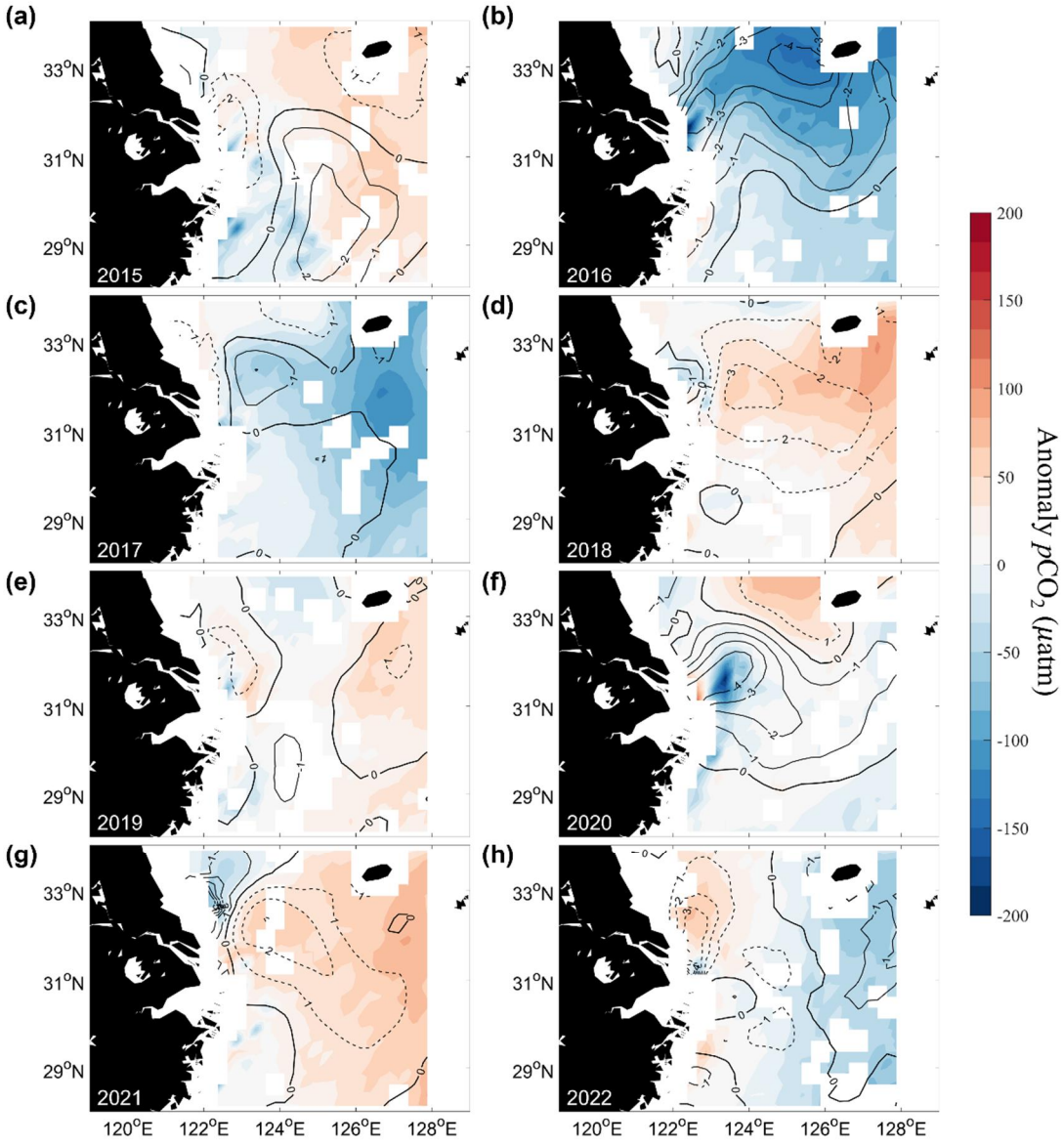

Figure 18. Same as Fig. 12 except for of pCO_2 anomaly (color) estimated from the combined use of SMAP SSS with satellite SST and *chl-a* concentration, based on MNR

There was an evident interconnection between pCO_2 and ocean environmental variables, as shown in Fig. 20, which indicated the comparison of the time series of pCO_2 with SST, SSS, and *chl-a* concentration. The ensemble means of SSS had a significant positive relationship with pCO_2, with a correlation coefficient of 0.83 (above a significant level of 99%). *chl-a* concentration exhibited an inverse correlation with pCO_2 (the correlation coefficient was -0.56, above a significant level of 90%). The extremely low pCO_2 level was found in 2016 when the combined effects of maximum riverine freshwater input, the primary production of phytoplankton biomass, and SST warming were intensive. These results agreed with the consequence of previous in situ observational-based studies (Liu et al., 2022, 2023), and in particular, the reduction of pCO_2 resulting from intensive biological activity in 2016 can be seen in the observation results (Choi et al., 2021).

These comparisons reveal that the riverine freshwater input containing high nutrient levels discharged from the Changjiang contributed to the reduction of surface pCO_2 anomaly over sea-surface freshening region. High nutrients promote the primary production of phytoplankton biomass within the surface layer, thus the enhanced biological activity can trigger the biological uptake of CO_2, leading to the drawdown of pCO_2. As shown in the result of 2016, the river-influenced SST warming also can help the biological CO_2 uptake in the surface layer by trapping primary production and weakening the surface mixing potentially.

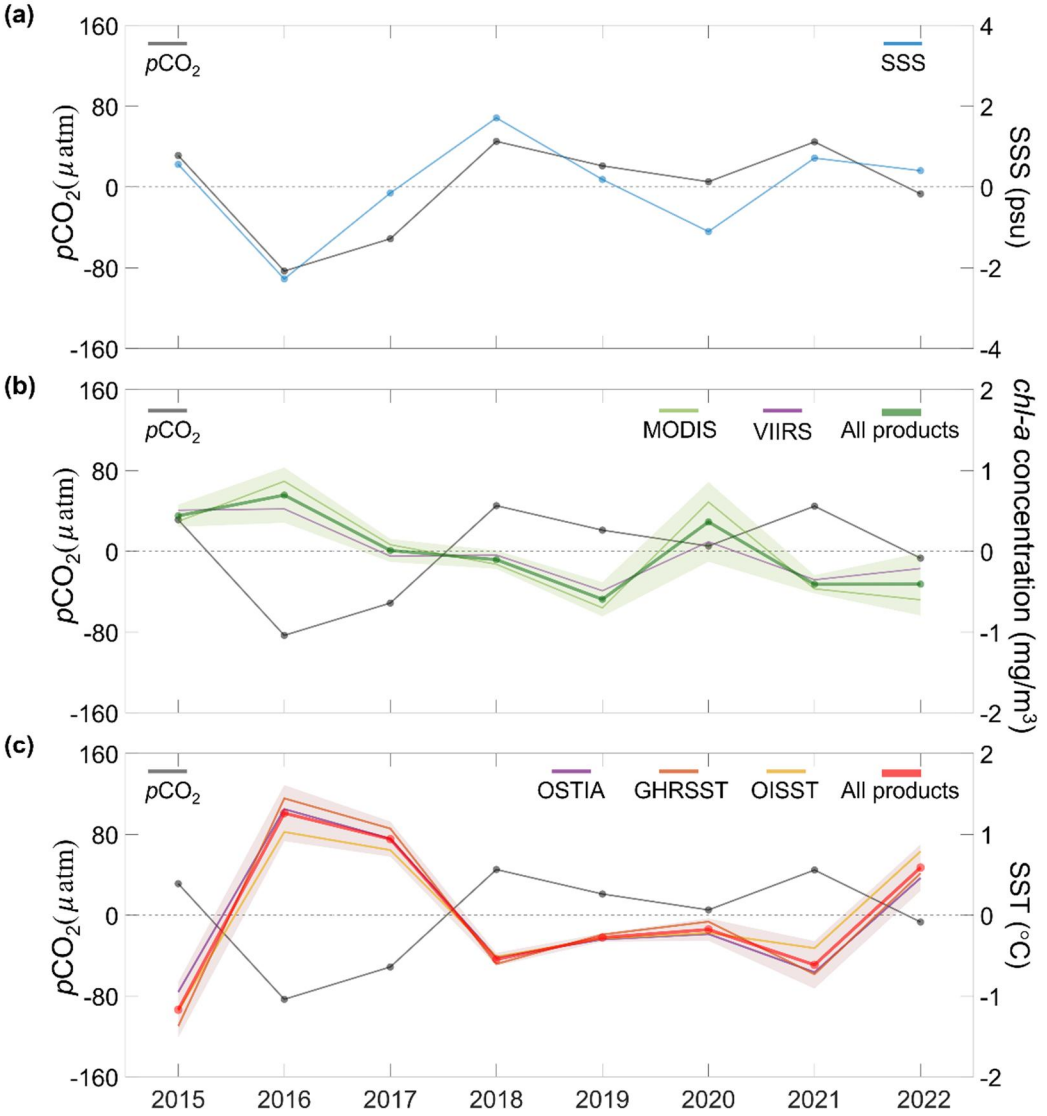

Figure 19. Comparisons of estimated pCO_2 anomaly with (a) SMAP SSS anomaly, (b) satellite SST anomalies and (c) satellite *chl-a* concentration anomalies in August from 2015 to 2022. The *chl-a* concentration anomalies derived from MODIS/Aqua and VIIRS products

6. Conclusion and Discussion

Monitoring SSS is important not only for the evaluation of ongoing changes in the ocean surface but also for providing insight into the ocean's role in hydrology and the carbon cycle. This is especially true in complex and highly dynamic river-dominated marginal seas because river discharge delivering terrestrial substances into the ocean plays a crucial role in controlling marine environments. In this study, we investigated how freshwater discharged from Changjiang affected the physical and biological responses and oceanic uptake of CO_2 by combining the recently available SSS product from the SMAP mission with other remote sensing measurements. First, an MLR approach with respect to SST, wind, and precipitation variables was applied to correct for seasonally dependent SMAP SSS bias and evaluated for the ECS, which is a river-dominated shelf region in the East Asian marginal seas. The impacts of riverine freshwater on the physicobiochemical ocean processes in terms of sea-surface warming, phytoplankton production, and oceanic CO_2 uptake were investigated by combining SMAP SSS with satellite SST and *chl-a* concentration datasets.

The primary mode of the bias-corrected SSS via CSEOF analysis represented a seasonal evolution of the SSS pattern that varied distinctly from year to year. The peak in the sea-surface freshening signal with the interannual mode occurred during times of high discharge in Changjiang, indicating the crucial role of riverine freshwater in the intensity of sea-surface freshening over the ECS shelf region in summer. Compared with SST and *chl-a* anomalies, we found that large amounts of freshwater discharged into the ECS tended to enhance SST warming and increase *chl-a* concentrations in the region where sea-surface freshening was robust. Under typical summer conditions with increased solar heating and calm wind states, the buoyant freshwater from Changjiang enhanced SST warming by trapping heat from the atmosphere in the shallow surface layer. The accompanying nutrient-rich freshwater promoted the production of phytoplanktons, which in turn led to *chl-a* enrichment in the ocean surface. A comparison with the estimated pCO_2 based on the MNR approach also

revealed a relationship between CO_2 uptake and satellite-derived environmental variables. During 2015-2022, relatively low pCO_2 appeared mostly in the region where SST warming and high *chl-a* concentrations were robust, highlighting that heat and riverine nutrients trapped within the buoyant plume contributed to the drawdown of pCO_2 by triggering the biological uptake of CO_2 in the surface layer.

Advances in our understanding of the impacts of riverine freshwater on surface environments have been demonstrated through the synergistic use of SMAP SSS with other satellite observations. While efforts to improve salinity remote sensing have been successful regarding spatial patterns, the short period covered by the SMAP record impedes a full understanding of the interannual to decadal variability of SSS and its impact on the marine environment, which plays a crucial role in both ecosystems and the carbon cycle. In addition, the correction of SMAP SSS used in this study effectively attenuated the seasonal dependence of SMAP bias due to the SST-related microwave sensor sensitivity for cold water conditions; however, it had little effect on the elimination of high-frequency signals, which may be associated with contamination by signals from land and RFI (Misra et al., 2013). Although the retrieval errors of space observations remain a concern, efforts to improve both retrieval algorithms and sensor technology and to accumulate a longer satellite SSS record will allow for better monitoring of SSS-related climate change and provide accurate datasets to estimate the global carbon cycle in the future.

List of References

Akhil, V.P., Vialard, J., Lengaigne, M., Keerthi, M.G., Boutin, J., Vergely, J.L., Papa, F., 2020. Bay of Bengal Sea surface salinity variability using a decade of improved SMOS re-processing. Remote Sens. Environ. 248, 111964. https://doi.org/10.1016/j.rse.2020.111964

Bai, Y., Cai, W.J., He, X.Q., Zhai, W.D., Pan, D.L., Dai, M.H., et al., 2015. A mechanistic semi-analytical method for remotely sensing sea surface pCO2 in river-dominated coastal oceans: a case study from the East China Sea. J. Geophys. Res. 120 (3), 2331–2349. https://doi.org/10.1002/2014JC010632.

Balaguru, K., Chang, P., Saravanan, R., Leung, L.R., Xu, Z., Li, M., Hsieh, J.-S., 2012. Ocean barrier layers' effect on tropical cyclone intensification. Proc. Natl. Acad. Sci. 109, 14343–14347. https://doi.org/10.1073/pnas.1201364109

Beardsley, R.C., Limeburner, R., Yu, H., Cannon, G.A., 1985. Discharge of the Changjiang (Yangtze River) into the East China Sea. Cont. Shelf Res., Sediment Dynamics of the Changjiang Estuary and the Adjacent East China Sea 4, 57–76. https://doi.org/10.1016/0278-4343(85)90022-6

Borges, A.V., Abril, G., Darchambeau, F., Teodoru, C.R., Deborde, J., Vidal, L.O., Lambert, T., Bouillon, S., 2015. Divergent biophysical controls of aquatic CO2 and CH4 in the World's two largest rivers. Sci. Rep. 5, 15614. https://doi.org/10.1038/srep15614

Boutin, J., Vergely, J.L., Marchand, S., D'Amico, F., Hasson, A., Kolodziejczyk, N., Reul, N., Reverdin, G., Vialard, J., 2018. New SMOS Sea Surface Salinity with reduced systematic errors and improved variability. Remote Sens. Environ. 214, 115–134. https://doi.org/10.1016/j.rse.2018.05.022

Cai, W.-J., Dai, M., 2004. Comment on "Enhanced Open Ocean Storage of CO2 from Shelf Sea Pumping." Science 306, 1477–1477. https://doi.org/10.1126/science.1102132

Chang, P.-H., Isobe, A., 2003. A numerical study on the Changjiang diluted water in the

Yellow and East China Seas. J. Geophys. Res. Oceans 108. https://doi.org/10.1029/2002JC001749

Chen, L., Xu, S., Gao, Z., Chen, H., Zhang, Y., Zhan, J., Li, W., 2011. Estimation of monthly air-sea CO2 flux in the southern Atlantic and Indian Ocean using in-situ and remotely sensed data. Remote Sens. Environ. 115, 1935–1941. https://doi.org/10.1016/j.rse.2011.03.016

Chen, S., Hu, C., Byrne, R.H., Robbins, L.L., Yang, B., 2016. Remote estimation of surface pCO2 on the West Florida Shelf. Cont. Shelf Res. 128, 10–25. https://doi.org/10.1016/j.csr.2016.09.004

Chen, S.L., Hu, C.M., Barnes, B.B., Wanninkhof, R., Cai, W.J., Barbero, L., et al., 2019. A machine learning approach to estimate surface ocean pCO2 from satellite measurements. Remote Sens. Environ. 228, 203–226. https://doi.org/10.1016/j.rse.2019.04.019.

Chin, T.M., Vazquez-Cuervo, J., Armstrong, E.M., 2017. A multi-scale high-resolution analysis of global sea surface temperature. Remote Sens. Environ. 200, 154–169. https://doi.org/10.1016/j.rse.2017.07.029

Choi, Y., Kim, D., Noh, J.H., Kang, D.-J., 2021. Contribution of Changjiang River discharge to CO2 uptake capacity of the northern East China Sea in August 2016. Cont. Shelf Res. 215, 104336. https://doi.org/10.1016/j.csr.2020.104336.

Chou, W.-C., Tishchenko, P.Y., Chuang, K.-Y., Gong, G.-C., Shkirnikova, E.M., Tishchenko, P.P., 2017. The contrasting behaviors of CO2 systems in river-dominated and ocean-dominated continental shelves: A case study in the East China Sea and the Peter the Great Bay of the Japan/East Sea in summer 2014. Mar. Chem., SI: Honoring Frank Millero 195, 50–60. https://doi.org/10.1016/j.marchem.2017.04.005

Dai, M., Su, J., Zhao, Y., Hofmann, E.E., Cao, Z., Cai, W.-J., Gan, J., Lacroix, F., Laruelle,

G.G., Meng, F., Müller, J.D., Regnier, P.A.G., Wang, G., Wang, Z., 2022. Carbon Fluxes in the Coastal Ocean: Synthesis, Boundary Processes, and Future Trends. Annu. Rev. Earth Planet. Sci. 50, 593–626. https://doi.org/10.1146/annurev-earth-032320-090746

Dinnat, E.P., Le Vine, D.M., Boutin, J., Meissner, T., Lagerloef, G., 2019. Remote Sensing of Sea Surface Salinity: Comparison of Satellite and In Situ Observations and Impact of Retrieval Parameters. Remote Sens. 11, 750. https://doi.org/10.3390/rs11070750

Donlon, C.J., Martin, M., Stark, J., Roberts-Jones, J., Fiedler, E., Wimmer, W., 2012. The Operational Sea Surface Temperature and Sea Ice Analysis (OSTIA) system. Remote Sens. Environ., Advanced Along Track Scanning Radiometer (AATSR) Special Issue 116, 140–158. https://doi.org/10.1016/j.rse.2010.10.017

Entekhabi, D., Njoku, E.G., O'Neill, P.E., Kellogg, K.H., Crow, W.T., Edelstein, W.N., Entin, J.K., Goodman, S.D., Jackson, T.J., Johnson, J., Kimball, J., Piepmeier, J.R., Koster, R.D., Martin, N., McDonald, K.C., Moghaddam, M., Moran, S., Reichle, R., Shi, J.C., Spencer, M.W., Thurman, S.W., Tsang, L., Van Zyl, J., 2010. The Soil Moisture Active Passive (SMAP) Mission. Proceedings of the IEEE 98, 704–716. https://doi.org/10.1109/JPROC.2010.2043918

Foltz, G. R., & McPhaden, M. J. 2009. Impact of barrier layer thickness on SST in the central tropical North Atlantic. J. Clim, 22(2), 285-299.

Fournier, S., & Lee, T. 2021. Seasonal and interannual variability of sea surface salinity near major river mouths of the world ocean inferred from gridded satellite and in-situ salinity products. Remote. Sens. 13(4), 728. https://doi.org/10.3390/rs13040728

Fournier, S., Vandemark, D., Gaultier, L., Lee, T., Jonsson, B., Gierach, M.M., 2017. Interannual Variation in Offshore Advection of Amazon-Orinoco Plume Waters: Observations, Forcing Mechanisms, and Impacts. J. Geophys. Res. Oceans 122, 8966–8982. https://doi.org/10.1002/2017JC013103

Franz, B. A., Werdell, P. J., Meister, G., Bailey, S. W., Eplee Jr, R. E., Feldman, G. C., ... & Kwiatkowska, E. J., McClain, C. R., Patt, F. S., Thomas, D. 2005. The continuity of ocean color measurements from SeaWiFS to MODIS. In Earth Observing Systems X (Vol. 5882, pp. 304-316). SPIE. https://doi.org/10.1117/12.620069

González-Gambau, V., Olmedo, E., Martínez, J., Turiel, A., Durán, I., 2017. Improvements on Calibration and Image Reconstruction of SMOS for Salinity Retrievals in Coastal Regions. IEEE Journal of Selected Topics in Applied Earth Observations and Remote Sensing 10, 3064–3078. https://doi.org/10.1109/JSTARS.2017.2685690

Grodsky, S.A., Reul, N., Bentamy, A., Vandemark, D., Guimbard, S., 2019. Eastern Mediterranean salinification observed in satellite salinity from SMAP mission. J. Mar. Syst. 198, 103190. https://doi.org/10.1016/j.jmarsys.2019.103190

Grodsky, S.A., Vandemark, D., Feng, H., 2018. Assessing Coastal SMAP Surface Salinity Accuracy and Its Application to Monitoring Gulf of Maine Circulation Dynamics. Remote Sens. 10, 1232. https://doi.org/10.3390/rs10081232

Hamlington, B.D., Cheon, S.H., Thompson, P.R., Merrifield, M.A., Nerem, R.S., Leben, R.R., Kim, K.-Y., 2016. An ongoing shift in Pacific Ocean sea level. J. Geophys. Res. Oceans 121, 5084–5097. https://doi.org/10.1002/2016JC011815

Hersbach, H., Bell, B., Berrisford, P., Biavati, G., Horányi, A., Muñoz Sabater, J., Nicolas, J., Peubey, C., Radu, R., Rozum, I., Schepers, D., Simmons, A., Soci, C., Dee, D., Thépaut, J-N. 2023: ERA5 monthly averaged data on single levels from 1940 to present. Copernicus Climate Change Service (C3S) Climate Data Store (CDS), DOI: 10.24381/cds.f17050d7 (Accessed on 01-May-2022)

Hong, J.-S., Moon, J.-H., Kim, T., You, S.H., Byun, K.-Y., Eom, H., 2022. Role of Salinity-Induced Barrier Layer in Air-Sea Interaction During the Intensification of a Typhoon. Front. Mar. Sci. 9, 844003. https://doi.org/10.3389/fmars.2022.844003

Hong, J.-S., Moon, J.-H., Lee, J.-H., Pang, I.-C., 2016. Modeling the largest inflow of

Changjiang freshwater into the Yellow Sea in 2012 with particle-tracking experiment. Ocean Sci. J. 51, 549–562. https://doi.org/10.1007/s12601-016-0057-1

Jiang, Z., Chen, J., Zhou, F., Shou, L., Chen, Q., Tao, B., Yan, X., Wang, K., 2015. Controlling factors of summer phytoplankton community in the Changjiang (Yangtze River) Estuary and adjacent East China Sea shelf. Cont. Shelf Res. 101, 71–84. https://doi.org/10.1016/j.csr.2015.04.009

Kako, S., Nakagawa, T., Takayama, K., Hirose, N., Isobe, A., 2016. Impact of Changjiang River Discharge on Sea Surface Temperature in the East China Sea. J. Phys. Oceanogr. 46, 1735–1750. https://doi.org/10.1175/JPO-D-15-0167.1

Kim, K.-Y., Hamlington, B., Na, H., 2015. Theoretical foundation of cyclostationary EOF analysis for geophysical and climatic variables: Concepts and examples. Earth-Science Reviews 150, 201–218. https://doi.org/10.1016/j.earscirev.2015.06.003

Kim, K. Y., & North, G. R. 1997. EOFs of harmonizable cyclostationary processes. Journal of the atmospheric sciences, 54(19), 2416-2427. https://doi.org/10.1175/1520-0469(1997)054<2416:EOHCP>2.0.CO;2

Köhler, J., Sena Martins, M., Serra, N., Stammer, D., 2015. Quality assessment of spaceborne sea surface salinity observations over the northern North Atlantic. J. Geophys. Res. Oceans 120, 94–112. https://doi.org/10.1002/2014JC010067

Kolodziejczyk, N., Boutin, J., Vergely, J.-L., Marchand, S., Martin, N., Reverdin, G., 2016. Mitigation of systematic errors in SMOS sea surface salinity. Remote Sens. Environ., Special Issue: ESA's Soil Moisture and Ocean Salinity Mission - Achievements and Applications 180, 164–177. https://doi.org/10.1016/j.rse.2016.02.061

Le Vine, D. M. 2019. RFI and remote sensing of the earth from space. J. Astron. Instrum., 8(1), 1–13. doi.org/10.1142/S2251171719400014

Le, C.F., Gao, Y.Y., Cai, W.J., Lehrter, J.C., Bai, Y., Jiang, Z.P., 2019. Estimating summer sea surface pCO2 on a river-dominated continental shelf using a satellite-based semi-

mechanistic model. Remote Sens. Environ. 225, 115–126. https://doi.org/10.1016/j.rse.2019.02.023.

Lie, H.-J., Cho, C.-H., Lee, J.-H., Lee, S., 2003. Structure and eastward extension of the Changjiang River plume in the East China Sea. J. Geophys. Res. Oceans 108. https://doi.org/10.1029/2001JC001194

Liu, J., Bellerby, R.G.J., Li, X., Yang, A., 2022. Seasonal Variability of the Carbonate System and Air–Sea CO2 Flux in the Outer Changjiang Estuary, East China Sea. Front. Mar. Sci. 8. https://doi.org/10.3389/fmars.2021.765564

Liu, J., Bellerby, R.G.J., Zhu, Q., Ge, J., 2023. Estimation of sea surface pCO2 and air–sea CO2 flux in the East China Sea using in-situ and satellite data over the period 2000–2016. Cont. Shelf Res. 254, 104879. https://doi.org/10.1016/j.csr.2022.104879

Meissner, T., 2018. NASA/RSS SMAP Salinity: Version 3.0 Validated Release. Remote Sensing Systems. https://doi.org/10.56236/RSS-bf

Meissner, T., Wentz, F.J., Scott, J., Vazquez-Cuervo, J., 2016. Sensitivity of Ocean Surface Salinity Measurements From Spaceborne L-Band Radiometers to Ancillary Sea Surface Temperature. IEEE Trans. Geosci. Remote Sens. 54, 7105–7111. https://doi.org/10.1109/TGRS.2016.2596100

Menezes, V. V. 2020. Statistical assessment of sea-surface salinity from SMAP: Arabian Sea, Bay of Bengal and a promising Red Sea application. Remote. Sens., 12(3), 1–37. doi.org/10.3390/rs12030447

Misra, S., Johnson, J., Aksoy, M., Peng, J., Bradley, D., O' Dwyer, I., Padmanabhan, S., Dawson, D., Chazanoff, S., Latham, B., Gaier, T., Flores-Helizon, C., Denning, R., 2013. SMAP RFI mitigation algorithm performance characterization using airborne high-rate direct-sampled SMAPVEX 2012 data, in: 2013 IEEE International Geoscience and Remote Sensing Symposium - IGARSS. Presented at the 2013 IEEE International Geoscience and Remote Sensing Symposium - IGARSS, pp. 41–44.

https://doi.org/10.1109/IGARSS.2013.6721087

Moon, J.-H., Kim, T., Son, Y.B., Hong, J.-S., Lee, J.-H., Chang, P.-H., Kim, S.-K., 2019. Contribution of low-salinity water to sea surface warming of the East China Sea in the summer of 2016. Prog. Oceanogr. 175, 68–80. https://doi.org/10.1016/j.pocean.2019.03.012

Moon, J.-H., Pang, I.-C., Yoon, J.-H., 2009a. Response of the Changjiang diluted water around Jeju Island to external forcings: A modeling study of 2002 and 2006. Cont. Shelf Res. 29, 1549–1564. https://doi.org/10.1016/j.csr.2009.04.007

Moon, J.-H., Song, Y.T., 2014. Seasonal salinity stratifications in the near-surface layer from Aquarius, Argo, and an ocean model: Focusing on the tropical Atlantic/Indian Oceans. J. Geophys. Res. Oceans 119, 6066–6077. https://doi.org/10.1002/2014JC009969

Moon, J. H., Hirose, N., & Yoon, J. H., 2009b. Comparison of wind and tidal contributions to seasonal circulation of the Yellow Sea. J. Geophys. Res. Oceans, 114(C8), https://doi.org/10.1029/2009JC005314

Moon, J. H., Hirose, N., Yoon, J. H., & Pang, I. C., 2010. Offshore detachment process of the low-salinity water around Changjiang Bank in the East China Sea. J. Phys. Oceanogr., 40(5), 1035-1053. https://doi.org/10.1175/2010JPO4167.1

Moon, J.H., Hirose, N., Pang, I.C., Hyun, K.H., 2012. Modeling offshore freshwater dispersal from the changjiang river and controlling factors during summer. Terr. Atmospheric Ocean. Sci. 23, 247–260. https://doi.org/10.3319/TAO.2012.01.10.01(Oc)

Moore, T.S., Campbell, J.W., Dowell, M.D., 2009. A class-based approach to characterizing and mapping the uncertainty of the MODIS ocean chlorophyll product. Remote Sens. Environ. 113, 2424–2430. https://doi.org/10.1016/j.rse.2009.07.016

Ono, T., T. Saino, N. Kurita, and K. Sasaki 2004, Basin-scale extrapolation of shipboard

pCO2 data by using satellite SST and Chla, Int. J. Remote Sens., 25(19), 3803– 3815, doi:10.1080/01431160310001657515.

Qin, S., Wang, Hui, Zhu, J., Wan, L., Zhang, Y., Wang, Haoyun, 2020. Validation and correction of sea surface salinity retrieval from SMAP. Acta Oceanol. Sin. 39, 148–158. https://doi.org/10.1007/s13131-020-1533-0

Rangama, Y., J. Boutin, J. Etcheto, L. Merlivat, T. Takahashi, B. Delille, M. Frankignoulle, and D. C. E. Bakker. 2005, Variability of the net air–sea CO2 flux inferred from shipboard and satellite measurements in the Southern Ocean south of Tasmania and New Zealand, J. Geophys. Res., 110, C09005, doi:10.1029/2004JC002619.

Reichle, R.H., G. De Lannoy, R.D. Koster, W.T. Crow, J.S. Kimball, Q. Liu, and M. Bechtold. 2022. SMAP L4 Global 3-hourly 9 km EASE-Grid Surface and Root Zone Soil Moisture Analysis Update, Version 7. Boulder, Colorado USA. NASA National Snow and Ice Data Center Distributed Active Archive Center. doi:10.5067/LWJ6TF5SZRG3

Reynolds, R. W., Smith, T. M., Liu, C., Chelton, D. B., Casey, K. S., & Schlax, M. G. 2007. Daily high-resolution-blended analyses for sea surface temperature. J. Clim., 20(22), 5473-5496. https://doi.org/10.1175/2007JCLI1824.1

Sarma, V. V. S. S., Saino, T., Sasaoka, K., Nojiri, Y., Ono, T., Ishii, M., Inoue, H.Y., Matsumoto, K. 2006. Basin□scale pCO2 distribution using satellite sea surface temperature, Chl a, and climatological salinity in the North Pacific in spring and summer. Global biogeochemical cycles, 20(3). doi.org/10.1029/2005GB002594

Scanlon, B. R., Rateb, A., Anyamba, A., Kebede, S., MacDonald, A. M., Shamsudduha, M., ... & Xie, H. 2022. Linkages between GRACE water storage, hydrologic extremes, and climate teleconnections in major African aquifers. Environmental Research Letters, 17(1), 014046.

Takahashi, T., Sutherland, S.C., Sweeney, C., Poisson, A., Metzl, N., Tilbrook, B., Bates, N., Wanninkhof, R., Feely, R.A., Sabine, C., Olafsson, J., Nojiri, Y., 2002. Global sea–air CO2 flux based on climatological surface ocean pCO2, and seasonal biological and temperature effects. Deep Sea Res. Part II Top. Stud. Oceanogr. 49, 1601–1622. https://doi.org/10.1016/S0967-0645(02)00003-6

Takahashi, T., Sutherland, S.C., Wanninkhof, R., Sweeney, C., Feely, R.A., Chipman, D.W., Hales, B., Friederich, G., Chavez, F., Sabine, C., Watson, A., Bakker, D.C.E., Schuster, U., Metzl, N., Yoshikawa-Inoue, H., Ishii, M., Midorikawa, T., Nojiri, Y., Körtzinger, A., Steinhoff, T., Hoppema, M., Olafsson, J., Arnarson, T.S., Tilbrook, B., Johannessen, T., Olsen, A., Bellerby, R., Wong, C.S., Delille, B., Bates, N.R., de Baar, H.J.W., 2009. Climatological mean and decadal change in surface ocean pCO2, and net sea-air CO2 flux over the global oceans. Deep-Sea Res. Part II Top. Stud. Oceanogr. 56, 554–577. https://doi.org/10.1016/j.dsr2.2008.12.009

Tang, W., Fore, A., Yueh, S., Lee, T., Hayashi, A., Sanchez-Franks, A., Martinez, J., King, B., Baranowski, D. 2017. Validating SMAP SSS with in situ measurements. Remote Sens. Environ., 200, 326-340. doi.org/10.1016/j.rse.2017.08.021

Tseng, C.-M., Liu, K.-K., Gong, G.-C., Shen, P.-Y., Cai, W.-J., 2011. CO 2 uptake in the East China Sea relying on Changjiang runoff is prone to change: THE ECS CO 2 UPTAKE IS PRONE TO CHANGE. Geophys. Res. Lett. 38, n/a-n/a. https://doi.org/10.1029/2011GL049774

Vinogradova, N., Lee, T., Boutin, J., Fournier, S., Sabia, R., Stammer, D., Bayler, E., Reul, N., Gordon, A., & Melnichenko, O., et al. 2019. Satellite salinity observing system: Recent discoveries and the way forward. Front. Mar. Sci, 6(243), 1–23. https://doi.org/10.3389/fmars.2019.00243

Wang, M., & Jiang, L. 2018. VIIRS-derived ocean color product using the imaging bands.

Remote sensing of environment, 206, 275-286.

Wang, M., Jiang, L., Liu, X., Son, S., Sun, J., Shi, W., Tan, L., Mikelsons, K., Wang, X., Lance, V., 2016. VIIRS ocean color products: A progress update, in: 2016 IEEE International Geoscience and Remote Sensing Symposium (IGARSS). Presented at the 2016 IEEE International Geoscience and Remote Sensing Symposium (IGARSS), pp. 5848–5851. https://doi.org/10.1109/IGARSS.2016.7730528

Wang, M., Liu, X., Jiang, L., Son, S., Sun, J., Shi, W., Tan, L., Naik, P., Mikelsons, K., Wang, X., Lance, V., 2014. Evaluation of VIIRS ocean color products, in: Ocean Remote Sensing and Monitoring from Space. Presented at the Ocean Remote Sensing and Monitoring from Space, SPIE, pp. 69–83. https://doi.org/10.1117/12.2069251

Whitney, M. M., & Garvine, R. W. (2005). Wind influence on a coastal buoyant outflow. J. Geophys. Res. Oceans, 110(C3). https://doi.org/10.1029/2003JC002261

Wu, H., Deng, B., Yuan, R., Hu, J., Gu, J., Shen, F., Zhu, J., Zhang, J., 2013. Detiding Measurement on Transport of the Changjiang-Derived Buoyant Coastal Current. J. Phys. Oceanogr. 43, 2388–2399. https://doi.org/10.1175/JPO-D-12-0158

Yeo, S.-R., Kim, K.-Y., 2015. Decadal changes in the Southern Hemisphere sea surface temperature in association with El Niño–Southern Oscillation and Southern Annular Mode. Clim. Dyn. 45, 3227–3242. https://doi.org/10.1007/s00382-015-2535-z

Yu, L., 2011. A global relationship between the ocean water cycle and near-surface salinity. J. Geophys. Res. Oceans 116. https://doi.org/10.1029/2010JC006937

Zhai, W., Dai, M., 2009. On the seasonal variation of air – sea CO2 fluxes in the outer Changjiang (Yangtze River) Estuary, East China Sea. Mar. Chem., 10th International Estuarine Biogeochemistry Symposium - “Estuaries in a Changing World” 117, 2–10. https://doi.org/10.1016/j.marchem.2009.02.008

Zhi, H., Zhang, R. H., Lin, P., Yu, P., Zhou, G., & Shi, S. 2020. Interannual salinity variability associated with the central Pacific and eastern Pacific El Niños in the

tropical Pacific. Journal of Geophysical Research: Oceans, 125(10), e2020JC016090.

Zhu, Z.-Y., Ng, W.-M., Liu, S.-M., Zhang, J., Chen, J.-C., Wu, Y., 2009. Estuarine phytoplankton dynamics and shift of limiting factors: A study in the Changjiang (Yangtze River) Estuary and adjacent area. Estuar. Coast. Shelf Sci., Marine Science in the Western Indian Ocean Responds to Population Pressures and Climate Change 84, 393–401. https://doi.org/10.1016/j.ecss.2009.07.005